

**Novel Nitridoborates: $M^{II}_2[BN_2]Br$ ($M^{II} = Ca, Sr, Eu$),
 $Eu_3[B_3N_6]$ and $Li_{0.42}Eu_3[B_3N_6]$
Synthesis, Crystal Structure and Physical Properties.**

by

Ilkin Kokal

**A Thesis Submitted to the
Graduate School of Engineering
in Partial Fulfillment of the Requirements for
the Degree of**

Master of Science

in

Material Science and Engineering

Koc University

September 2008

Koc University

Graduate School of Sciences and Engineering

This is to certify that I have examined this copy of a master's thesis by

Ilkin Kokal

and have found that it is complete and satisfactory in all respects,
and that any and all revisions required by the final
examining committee have been made.

Committee Members:

Mehmet Somer, Ph. D. (Advisor)

Peter Höhn, Ph. D.

Funda Yagci Acar , Ph. D.

Date: 17.09.2008

ABSTRACT

The isostructural compound series $M^{II}_2[BN_2]Br$ ($M^{II} = Ca, Sr, Eu$) crystallize in the rhombohedral space group $R\bar{3}m$ (Pearson code $hR6$; $Z = 3$) with $a = 3.86897(7)\text{\AA}$, $c = 25.8135(6)\text{\AA}$ for $Ca_2[BN_2]Br$, $a = 4.117\text{\AA}$, $c = 26.487$ for $Sr_2[BN_2]Br$ and $a = 4.0728\text{\AA}$, $c = 26.5890\text{\AA}$ for $Eu_2[BN_2]Br$. The crystal structure can be interpreted as a filled variant of anti- $NaCrS_2$ type of structure in which M at S positions, Br at Cr positions and B at Na positions. The structure is characterized by slabs of edge-sharing $[N-B-N]@M_6$ and $[Br]@M_6$ trigonal antiprisms which are alternately packed along $[001]$. The bond lengths for the strictly linear $[BN_2]^{3-}$ anions vary only marginal: $d(B-N) = 1.353(7) - 1.355(4)\text{\AA}$ and are directly comparable with those of the other well-known dinitrido borates and -halides. Unlike the isostoichiometric dinitridoborate bromide series, $Eu_2[BN_2]I$ crystallizes monoclinic (space group: $P2_1/m$ (No:11) with $a = 10.2548\text{\AA}$, $b = 4.1587\text{\AA}$, $c = 13.1234\text{\AA}$, $\beta = 91.21$, $Z = 4$, $V = 559.54\text{\AA}^3$) and is isotypic to $Sr_2[BN_2]I$. The crystal structure consists of slightly corrugated layers of condensed $I@Eu_6$ octahedra which are separated by isolated $[BN_2]^{3-}$ anions. The bond lengths for the crystallographically distinct $[BN_2]^{3-}$ moieties are: $d(B1-N3) = 1.301(39)\text{\AA}$, $d(B1-N4) = 1.352(36)\text{\AA}$, $d(B2-N1) = 1.302(49)\text{\AA}$ and $d(B2-N2) = 1.348(48)\text{\AA}$, respectively. The bond angles differ significantly from the linearity: $\angle(N3-B1-N4) = 178.92(3)^\circ$ and $\angle(N1-B2-N2) = 172.90^\circ(4)$. Vibrational Spectra confirm the presence of the $[N-B-N]^{3-}$ units in all four nitridoborate halides. According to the magnetic susceptibility measurements the oxidation state of Eu in $Eu_2[BN_2]X$ ($X = Br, I$) is +2.

$Eu_3[B_3N_6]$ and $Li_{0.42}Eu_3[B_3N_6]$ crystallize in the trigonal space group $R\bar{3}c$ (No:167) with $a = 11.9559(2)\text{\AA}$, $c = 6.814(2)\text{\AA}$ and $Z = 6$ for $Eu_3[B_3N_6]$ and $a = 12.0225(2)\text{\AA}$, $c = 6.8556(2)\text{\AA}$ and $Z = 6$ for $Li_{0.42}Eu_3[B_3N_6]$. Partial anionic structures are built up by isolated, planar cyclic $[B_3N_6]^{9-}$ units ($d(B-N)_{exo} = 1.466(2)$, $d(B-N)_{endo} = 1.475(4)$) which

are surrounded by bi capped polyhedra of trivalent Eu for $\text{Eu}_3[\text{B}_3\text{N}_6]$ and mixed valent $\text{Eu}^{3+}/\text{Eu}^{2+}$ for $\text{Li}_{0.42}\text{Eu}_3[\text{B}_3\text{N}_6]$, respectively. In $\text{Li}_{0.42}\text{Eu}_3[\text{B}_3\text{N}_6]$, Li^+ occupies statistically (42%) the sites $36f$ and is sandwiched between the $[\text{B}_3\text{N}_6]^{9-}$ anions. The oxidation state +3 for Eu in $\text{Eu}_3[\text{B}_3\text{N}_6]$ and mixed valance state (+2/+3) in $\text{Li}_{0.42}\text{Eu}_3[\text{B}_3\text{N}_6]$ are verified by magnetic measurements, ESR and Mössbauer Spectroscopy.

ÖZET

Benzer yapıdaki bileşik serisi $M^{II}_2[BN_2]Br$ ($M^{II} = Ca, Sr, Eu$) rombohedral uzay grubunda $R\bar{3}m$ (Pearson code $hR6$; $Z = 3$) $a = 3.86897(7)\text{Å}$, $c = 25.8135(6)\text{Å}$ $Ca_2[BN_2]Br$, için $a = 4.117\text{Å}$, $c = 26.487$ $Sr_2[BN_2]Br$ için ve $Eu_2[BN_2]Br$ $a = 4.0728\text{Å}$, $c = 26.5890\text{Å}$ hücresel parametreleri ile kristalleşmektedir. Kristal yapılar anti- $NaCrS_2$ bileşiğinin doldurulmuş varyasyonudur. M^{II} katyonları S pozisyonunda ve sırasıyla Br ve B da Cr ve Na pozisyonlarındadır.

Diğer bir bileşik olan $Eu_2[BN_2]I$ monoklinik yapıda ve $a = 10.2548\text{Å}$, $b = 4.1587\text{Å}$, $c = 13.1234\text{Å}$, $\beta = 91.21$, $Z = 4$, $V = 559.54\text{Å}^3$) hücresel parametreleri ile kristallenir. Bu yapılarda belirgin gruplar izole ve çubuk yapıdaki $[N-B-N]^3$ ve küresel X^- anyonlardır.

Bileşiklerdeki $[N-B-N]^3$ yapılar titreşim spektroskopisi ile belirlenmiş olup. Eu katyonlarının da değerlikleri manyetik ölçümler ile incelenmiştir.

$Eu_3[B_3N_6]$ (1) ve $Li_{0.42}Eu_3[B_3N_6]$ (2) $R\bar{3}c$ (No:167) trigonal uzay grubunda sırası ile $a = 11.9559(2)\text{Å}$, $c = 6.814(2)\text{Å}$ ve $Z = 6$ (1) ve $a = 12.0225(2)\text{Å}$, $c = 6.8556(2)\text{Å}$ ve $Z = 6$ (2) hücresel parametreleri ile kristalize olurlar. $Eu_3[B_3N_6]$ bileşiği düzeysel ve dairesel $[B_3N_6]^{9-}$ grupları ve bunları saran +3 değerlikli Eu katyonlarından $Li_{0.42}Eu_3[B_3N_6]$ bileşiği ise etrafı iki değerlikli (Eu^{3+}/Eu^{2+}) katyonları ile sarılı düzeysel ve dairesel $[B_3N_6]^{9-}$ ünitelerinden oluşmuştur. $Li_{0.42}Eu_3[B_3N_6]$ bileşiğinde, Li^+ 36 f pozisyonunu istatistiksel olarak (42%) doldurmakta ve $[B_3N_6]^{9-}$ grupları arasında sıkışmıştır. $Eu_3[B_3N_6]$ ve $Li_{0.42}Eu_3[B_3N_6]$ bileşiklerindeki Eu katyonlarının değerlikleri manyetik ölçümler, ESR ve Mössbauer spektroskopisi yöntemleri ile incelenmiştir.

ACKNOWLEDGEMENTS

I would like to thank my advisor Prof. Dr. Mehmet Somer giving me a chance to work in his research group and his help during my study. It was a great chance for me to start an academic career under his supervision. I have learned and achieved more than I ever dreamed of in two-years by his precious guiding and help, and I feel myself very lucky and very proud of being one of his students.

My special thanks goes to Dr. Peter Hohn, who gave me the opportunity to work in MPI-CPfS Dresden and the possibility to complete my thesis.

Thanks are also to the people at MPI-CPfS who have helped me towards the completion of my M.S thesis work. I would like to thank, Dr. Y. Prots and Dr. L Akselrud for providing me X-ray diffraction measurements and many fruitful discussions about crystallography. Thanks to Dr. W. Schnelle for the physical property measurements and interpretation of them. I also want to thank Umut Aydemir, because of his kind assistance, giving wise advice, helping with various applications, and more important being a very good friend. I also thank to TUBITAK (The Scientific and Technological Research Council of Turkey) for their generous financial support.

I am grateful to all my friends at Inorganic Lab group and my best friends; Selçuk Acar, Semih Afyon, Tolga Bayrak, Çınar Erganli, Ismail Filiz, Kâmil Kiraz, Süleyman Sinan Öztürk for their valuable friendship, and for all the fun and good times we shared together.

The last but not least, I thank my parents and sister for believing in me and trusting me at every step I have taken so far. I am very lucky to be a part of such a wonderful family.

TABLE OF CONTENTS

List of Tables	ix
List of Figures	xi
Nomenclature	xiv
Chapter 1: Introduction	1
Chapter 2: Experimental Techniques	8
2.1 Introductory Remarks	8
2.2 Material and Chemical Used, Sources and Quality	8
2.3 Experimental Methods	10
2.3.1 Gas Purification System and Glove Box	10
2.3.2 High Temperature Annealing in Quartz Tube and Sealed Ampoules	11
2.4 Materials Characterization	11
2.4.1 X-Ray Diffraction Techniques	11
2.4.2 Differential Thermal Analysis(DTA).	13
2.4.3 Infrared Spectroscopy	14
2.4.4 Raman Spectroscopy	15
2.4.5 Electron Spin Resonance Spectroscopy(ESR)	15
2.4.6 Mossbauer Spectroscopy	16
2.4.6 Magnetic Measurements.	17

Chapter 3: $M^{II}_2[BN_2]Br$ ($M^{II} = Ca, Sr, Eu$)	18
3.1 Synthesis	18
3.2 Crystal Structure	21
3.3 Physical Properties.	29
3.3.1 Infrared and Raman Spectroscopy	29
3.3.2 Differential Thermal Analysis	31
3.3.3 Magnetic Susceptibility	36
Chapter 4: $Eu_2[BN_2]I$	38
4.1 Synthesis	38
4.2 Crystal Structure	39
4.3 Physical Properties.	44
4.3.1 Infrared and Raman Spectroscopy	44
4.3.2 Magnetic Susceptibility	45
Chapter 5: $Eu_3[B_3N_6]$ and $Li_{0.42}Eu_3[B_3N_6]$	47
5.1 Synthesis	47
5.2 Crystal Structure	49
5.3 Physical Properties.	56
5.3.1 Magnetic Susceptibility	56
5.3.2 Electron Spin Resonance Spectroscopy	58
5.3.3 Mossbauer Spectroscopy.	61
Chapter 6: Conclusions	63
Bibliography	66
Vita	69

LIST OF TABLES

Table 1. 1 Nitridoborates with discrete [N-B-N] ³⁻ units.....	1
Table 1. 2 Nitridoborates Halides with discrete [N-B-N] ³⁻ units.....	3
Table 2. 1 Chemicals used and their specifications	9
Table 3. 1 Crystallographic data and, refinement details for M ^{II} ₂ [BN ₂]Br (M ^{II} = Ca, Sr, Eu)	25
Table 3. 2 Atomic coordinates and displacement parameters of [in Å ²] for Ca ₂ [BN ₂]Br	26
Table 3. 3 Anisotropic displacement parameters [10 ⁻⁴ pm ²] for Ca ₂ [BN ₂]Br, standard deviations of the last digit in parentheses	26
Table 3. 4 Atomic coordinates and displacement parameters of [in Å ²] for Sr ₂ [BN ₂]Br	27
Table 3. 5 Anisotropic displacement parameters [10 ⁻⁴ pm ²] for Sr ₂ [BN ₂]Br, standard deviations of the last digit in parentheses	27
Table 3. 6 Atomic coordinates and displacement parameters of [in Å ²] for Eu ₂ [BN ₂]Br	27
Table 3. 7 Anisotropic displacement parameters [10 ⁻⁴ pm ²] for Eu ₂ [BN ₂]Br, standard deviations of the last digit in parentheses	27
Table 3. 8 Selected atomic distances [Å] and bond angles [°] in Ca ₂ [BN ₂]Br with their multiplicity (n).....	28
Table 3. 9 Selected atomic distances [Å] and bond angles [°] in Sr ₂ [BN ₂]Br with their multiplicity (n).....	28
Table 3. 10 Selected atomic distances [Å] and bond angles [°] in Eu ₂ [BN ₂]Br with their multiplicity (n).....	28
Table 4. 1 Crystallographic data and, refinement details for Eu ₂ [BN ₂]I.....	42

Table 4. 2 Atomic coordinates and displacement parameters of [in Å ²] for Eu ₂ [BN ₂]I.....	42
.....	
Table 4. 3 Anisotropic displacement parameters [10 ⁻⁴ pm ²] for Eu ₂ [BN ₂]I, standard deviations of the last digit in parentheses	43
Table 4. 4 Selected atomic distances [Å] and bond angles [°] in Eu ₂ [BN ₂]I with their multiplicity (n).....	43
Table 5. 1 Crystallographic data and, refinement details for Eu ₃ [B ₃ N ₆] and Li _{0.42} Eu ₃ [B ₃ N ₆]	54
.....	
Table 5. 2 Atomic coordinates and displacement parameters of [in Å ²] for Eu ₃ [B ₃ N ₆]	54
.....	
Table 5. 3 Atomic coordinates and displacement parameters of [in Å ²] for Li _{0.42} Eu ₃ [B ₃ N ₆]	55
.....	
Table 5. 4 Selected atomic distances [Å] and bond angles [°] in Eu ₃ [B ₃ N ₆] with their multiplicity (n).....	55
Table 5. 5 Selected atomic distances [Å] and bond angles [°] in Li _{0.42} Eu ₃ [B ₃ N ₆] with their multiplicity (n).....	55
Table 5. 6 Anisotropic displacement parameters [10 ⁻⁴ pm ²] for Eu ₃ [B ₃ N ₆], standard deviations of the last digit in parentheses	56
Table 5. 7 Anisotropic displacement parameters [10 ⁻⁴ pm ²] for Li _{0.42} Eu ₃ [B ₃ N ₆], standard deviations of the last digit in parentheses	56

LIST OF FIGURES

Figure 2. 1 MBraun Gas Purification and Glove Box[MBraun].	10
Figure 2. 2 X-ray Sample Holder and Polyimid (Kapton) film for moisture sensitive samples.....	13
Figure 2. 3 Setup for preparing 13mm pellet for IR measurement	15
Figure 2. 4 Calibrated thin walled quartz tube for ESR measurements	16
Figure 2. 5 Calibrated thin walled quartz tube for Magnetic susceptibilitiy measurements	17
Figure 3. 1. 1 Observed and calculated X-ray Powder Diffraction patterns of $\text{Ca}_2[\text{BN}_2]\text{Br}$	19
Figure 3. 1. 2 Observed and calculated X-ray Powder Diffraction patterns of $\text{Sr}_2[\text{BN}_2]\text{Br}$	20
Figure 3. 1. 3 Observed and calculated X-ray Powder Diffraction patterns of $\text{Eu}_2[\text{BN}_2]\text{Br}$	21
Figure 3. 2. 1 Crystal Structure of $\text{M}^{\text{II}}_2[\text{BN}_2]\text{Br}$ ($\text{M}^{\text{II}} = \text{Ca}, \text{Sr}, \text{Eu}$).....	23
Figure 3. 2. 2 Crystal Structure of $\text{M}^{\text{II}}_2[\text{BN}_2]\text{Br}$ ($\text{M}^{\text{II}} = \text{Ca}, \text{Sr}, \text{Eu}$).....	24
Figure 3. 2. 3 Trigonal anti prismatic coordination of M around Br atoms in the crsytal structures of $\text{M}^{\text{II}}_2[\text{BN}_2]\text{Br}$ ($\text{M}^{\text{II}} = \text{Ca}, \text{Sr}, \text{Eu}$).....	25
Figure 3. 3. 1 Vibrational Spectra of $\text{Ca}_2[\text{BN}_2]\text{Br}$	29
Figure 3. 3. 2 Vibrational Spectra of $\text{Sr}_2[\text{BN}_2]\text{Br}$	30
Figure 3. 3. 3 Vibrational Spectra of $\text{Eu}_2[\text{BN}_2]\text{Br}$	31
Figure 3. 3. 4 Differential Thermal Analysis curve of the starting mixtures for $\text{Ca}_2[\text{BN}_2]\text{Br}$, heated up to 1600K	32
Figure 3. 3. 5 Powder X-ray diffraction pattern of DTA sample of $\text{Ca}_2[\text{BN}_2]\text{Br}$ after cooling from 1600K.....	33

Figure 3. 3. 6 Differential Thermal Analysis curve of the starting mixtures for Sr ₂ [BN ₂]Br, heated up to 1600K	34
Figure 3. 3. 7 Powder X-ray diffraction pattern of DTA sample of Sr ₂ [BN ₂]Br after cooling from 1600K.....	35
Figure 3. 3. 8 Temperature dependence of the reciprocal magnetic susceptibilities of Eu ₂ [BN ₂]Br determined at a magnetic flux density of 1T	36
Figure 4. 1. 1 Observed and calculated X-ray Powder Diffraction patterns of Eu ₂ [BN ₂]I.....	39
Figure 4. 2. 1 Crystal Structure of Eu ₂ [BN ₂]I.....	41
Figure 4. 3. 1 Vibrational Spectra of Eu ₂ [BN ₂]I	45
Figure 4. 3. 2 Temperature dependence of the reciprocal magnetic susceptibilities of Eu ₂ [BN ₂]I determined at a magnetic flux density of 1T.....	46
Figure 5. 1. 1 Observed and calculated X-ray Powder Diffraction patterns of Eu ₃ [B ₃ N ₆].....	48
Figure 5. 1. 2 Observed and calculated X-ray Powder Diffraction patterns of Li _{0.42} Eu ₃ [B ₃ N ₆].....	49
Figure 5. 2. 1 Crystal Structure of Eu ₃ [B ₃ N ₆].....	50
Figure 5. 2. 2 Tetrahedral coordination of Eu and B around endo-cyclic N	50
Figure 5. 2. 3 Cyclic [B ₃ N ₆] ⁹⁻ units and polyhedra	51
Figure 5. 2. 4 Local coordination for Eu	51
Figure 5. 2. 5 Crystal Structure of Li _{0.42} Eu ₃ [B ₃ N ₆].....	52
Figure 5. 2. 6 Cyclic [B ₃ N ₆] ⁹⁻ units in the structure	53
Figure 5. 3. 1 Temperature dependence of the reciprocal magnetic susceptibilities of Eu ₃ [B ₃ N ₆] determined at a magnetic flux density of 1T.....	57
Figure 5. 3. 2 Temperature dependence of the reciprocal magnetic susceptibilities of Li _{0.42} Eu ₃ [B ₃ N ₆] determined at a magnetic flux density of 3.5T.....	58

Figure 5. 3. 3 Electron Spin Resonance spectra of $\text{Li}_{0.42}\text{Eu}_3[\text{B}_3\text{N}_6]$ (black) and $\text{Eu}_3[\text{B}_3\text{N}_6]$ (red) at 294K	59
Figure 5. 3. 4 The X-band ESR spectra of $\text{Li}_{0.42}\text{Eu}_3[\text{B}_3\text{N}_6]$ at 294K is presented together with the temperature dependency of g factor.....	60
Figure 5. 3. 5 The ^{151}Eu Mössbauer spectra of $\text{Eu}_3[\text{B}_3\text{N}_6]$ at 78 K is presented together with a transmission integral fits.	61
Figure 5. 3. 6 The ^{151}Eu Mössbauer spectra of $\text{Eu}_3[\text{B}_3\text{N}_6]$ at 78 K is presented together with a transmission integral fits.	62




NOMENCLATURE




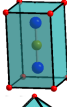
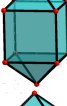


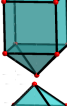
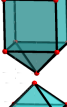
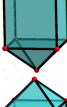

DTA	:	Differential Thermal Analysis
DSC	:	Differential Scanning Calorimetry
XRD	:	X-Ray Diffraction
IR	:	Infra Red
ESR	:	Electron Spin Resonance Spectroscopy
Nd:YAG	:	Neodymium doped yttrium aluminum garnet
Goof	:	Goodness of fit
CN	:	Coordination Number
n	:	Number of Reflections
R	:	Residual or agreement index
U_{eq}	:	Isotropic mean-square displacement parameter
Z	:	Number of formula units
χ	:	Magnetic susceptibility
Θ	:	Curie- Weiss constant
μ_{eff}	:	Effective magnetic moment
δ	:	Isomer Shift
Γ	:	Line Width
λ	:	Wavelength of the incident beam
h	:	Boltzmann constant
v	:	Bohr Frequency

Chapter 1

INTRODUCTION

Compounds with the discrete linear dinitridoborate anions $[\text{N}=\text{B}=\text{N}]^{3-}$, isoelectronic to CO_2 , have been first reported by Goubeau und Anselment in 1961 [1]. In 1983 Sato et al. [2] discovered the catalytical role of the ternary dinitridoborates of alkali and earth alkaline metals in conversion of hexagonal boron nitride (h-BN) to cubic boron nitride (c-BN) with diamond structure. This discovery opened an interesting research area with a great many novel compounds listed in Table 1 and Table 2, comprising beside the linear $[\text{BN}_2]^{3-}$ moieties also isolated halides, and hydride anions as characteristic structural units.

Nitrido Borate	Space Group	Nitrogen cor.	$[\text{BN}_2]^{3-}$ (CN)	Lit.
$\alpha\text{-Li}_3[\text{BN}_2]$	$P2_1/c$ (No.14)	Irregular (very distorted square anti-prism)	8	[3]
$\beta\text{-Li}_3[\text{BN}_2]$	$P42/mnm$ (No.136)		10	[3]
$\text{Na}_3[\text{BN}_2]$	$P2_1/c$ (No.14)	Irregular (very distorted square anti-prism)	8	[4]
$\alpha\text{-Ca}_3[\text{BN}_2]_2$	$Im\bar{3}m$ (No.229)		10	[5]
$\beta\text{-Ca}_3[\text{BN}_2]_2$	$Cmca$, (No.64)		10	[6]

α -Sr ₃ [BN ₂] ₂	$Im\bar{3}m$ (No.229)		10	[7]
β -Sr ₃ [BN ₂] ₂	$Pm\bar{3}m$ (No.229)		Linear	[8]
α -Ba ₃ [BN ₂] ₂	$P2_12_12_1$ (No.19)	Very Irregular Bi-caped Trigonal prism	8	[9]
β -Ba ₃ [BN ₂] ₂	$Im\bar{3}m$ (No.229)		10	[9]
LiMg[BN ₂]	$I4/mmm$ (No.139)		8	[10]
LiCa ₄ [BN ₂] ₃	$Im\bar{3}m$ (No.229)		10	[11]
LiSr ₄ [BN ₂] ₃	$Im\bar{3}m$ (No.229)		10	[12]
LiBa ₄ [BN ₂] ₃	$Im\bar{3}m$ (No.229)		10	[13]
LiEu ₄ [BN ₂] ₃	$Im\bar{3}m$ (No.229)		10	[14]
NaSr ₄ [BN ₂] ₃	$Im\bar{3}m$ (No.229)		10	[13]
NaBa ₄ [BN ₂] ₃	$Im\bar{3}m$ (No.229)		10	[15]
Mg _{2-x} Ae _{8-y} [BN ₂] ₆ (Ae = Ca,Sr,Ba)	$Im\bar{3}m$ (No.229)		10	[16]




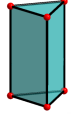

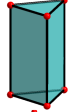


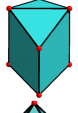

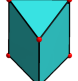
CaM₈[BN₂]₆ (M = Sr, Ba, Eu)	$Im\bar{3}m$ (No.229)		10	[16]
MBa₈[BN₂]₆ (M = Sr, Eu)	$Im\bar{3}m$ (No.229)		10	[17]

Table 1.1 Nitridoborates with discrete [N-B-N]³⁻ units.

Nitrido Borate	Space Group	Nitrogen cor.	[BN ₂] ³⁻ (CN)	X ⁻ (CN)	Lit.
Mg₄[BN₂]N_{1.5}F_{0.5}	$R\bar{3}m$ (No.166)		6	5	[18]
Mg₂[BN₂]Cl	$Pbca$, (No.61)		6	7	[19]
Mg₂[BN₂]Br	$C2/c$, (No.15)		6	6	[18]
Mg₈[BN₂]I	$Imma$ (No.74)		6	14+2	[19]
Ca₂[BN₂]H	$Pnma$, (No.62)		8	4	[20]
Ca₂[BN₂]F	$Pnma$, (No.62)		8	4	[21]
Ca₂[BN₂]Cl	$Pnma$, (No.62)		6+1	5	[21]
Sr₂[BN₂]F	$Pnma$, (No.62)		8	4	[21]
Sr₂[BN₂]Cl	$Pnma$, (No.62)		6+1	5	[21]

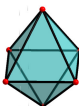
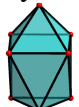
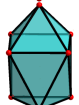
Sr₂[BN₂]I	$P2_1/m, (No.11)$		6	6	[22]
Ba₈[BN₂]₅F	$P\bar{1}, (No.2)$	Irregular 1-4-3 polyhedra	8	4	[23]
Ba₂[BN₂]Cl	$I4_132, (No.214)$		8	4	[24]
Ba₂[BN₂]Br	$I4_132, (No.214)$		8	4	[25]

Table 1.2 Nitridoborate Halides with discrete [N-B-N]³⁻ units

A remarkable feature of the compounds depicted in this list is that almost all of the pure dinitridoborates and their derivatives are formed exclusively in presence of mono and divalent cations of alkali and earth alkaline metals and their combinations. An exception is Eu(II) which is known to behave crystal-chemically like Sr²⁺. Not included in the Table 1 are nitridoborates with trivalent rare earth metals such as La, Ce and Pr. In this case, however, the linear units (N=B=N) either oligomerize to form the cyclic [B₃N₆]⁹⁻ isosteric to [B₃O₆]³⁻ or decompose yielding trigonal planar [BN₃]⁶⁻ or B₂Cl₄ analogue [B₂N₄]⁶⁻ moieties with comparatively short (B-B) bonds.

While alkali metal dinitridoborates Na₂BN₂ and Li₃BN₂ crystallize monoclinic or teragonal (α -Li₃BN₂), the compounds series M^{II}₃[BN₂]₂ (M^{II} = Ca, Sr, Ba, Eu) and M^I(M^{II})₄[BN₂] (M^I = Li, Na; M^{II} = Ca, Sr, Ba, Eu) prefer a cubic symmetry. The crystal structure of the latter can be described as a filled variant of the well-known HgPt₂ type of structure. The cationic partial structure M^I(M^{II})₄ consists M^{II}₈ cubes centered by M^I atoms which are further condensed to form a 3D frame work. The empty holes of the cube are filled by [BN₂]³⁻ units.

In the case of the pure $M^{II}_3[BN_2]_2$, the M^I positions are statistically only half occupied by the divalent M^{II} . Thus, a filled structure can only be achieved by an increase of the anionic charge as been realized for $Ca_{10}[BN_2]_4[CBN]_2$, obtained by a high temperature reaction of $Ca_3[BN_2]_2$ with elemental carbon. The doping attempts of the cubic compounds with metals such Al, Ge, Fe etc. lead to significant changes of the physical properties such as color and conductivity while the crystal structure is more or less maintained. More exciting, however, are the reactions of the $M^{II}_3[BN_2]_2$ ($M^{II} = Ca, Sr, Ba, Eu$) series with metal halides, oxides or hydrides, resulting in the breakdown of the cubic structure and formation of a new class of compounds, comprising both linear $[N=B=N]^{3-}$ and spherical X^{n-} anions ($X = F, Cl, Br, I; H; O; N = 1, 2$). Among these so called double salts, the best investigated ones are the dinitridoborate halides with the general composition $M^{II}_2[BN_2]X$ ($M = Mg, Ca, Sr, Ba, Eu; X = F, Cl, Br, I$). The existence of an earth alkaline dinitridoborate halide was first discovered by Meyer et al. [5] while the first systematic investigations are stemming from Rohrer and Nesper et al. [21, 22, 23]. Their extensive study on $M^{II} \text{halide}/(M^{II})_3N_2/BN$ system with $M^{II} = Ca, Sr$ and Ba led to an array of hitherto unknown compounds with a surprising variety of structural arrangements, as can be seen in Table. 2. These studies were completed by the recent investigations on the missing magnesium phases whose compositions and crystal structures are also presented in Tab. 2. Although most of these double salts are isostoichiometric, only very few of them are isostructural. The structural variety is due to complex packing effects and must be considered as a compromise about how to pack spherically shaped halogenide and the rod-like nitridoborate anions in a reasonable manner. The common structural guideline in all these phases is the distinct separation between the substructures of halides and dinitridoborate anions. Another important factor effecting the structural variety are the ionic sizes, and particularly those of the large halides, while the size of the (BN_2) moieties can be regarded as uniform. The size of the earth alkaline cations plays also a role, but their

contribution is much less emphasized. The local structures of metals around the halogen atoms show a broad range of coordination numbers, ranking between tetrahedral (CN4) and tpb (CN5) for the small fluorides and CN6 ($\text{Mg}_2[\text{BN}_2]\text{Br}$) to CN(2+10) ($\text{Mg}_8[\text{BN}_2]_5\text{I}$) for the large iodides. The largest diversity of coordination is revealed by the chloride ions between CN4 for $\text{Ba}_2[\text{BN}_2]\text{Cl}$ and CN7 for $\text{Mg}_2[\text{BN}_2]\text{Cl}$. The coordination geometry around bromide varies between CN4 - distorted tetrahedron - ($\text{Ba}_2[\text{BN}_2]\text{Br}$) and CN6 - very distorted trigonal prism- ($\text{Mg}_2[\text{BN}_2]\text{Br}$).

As a result of strong packing effects and cation-anion interactions in the crystal, the $[\text{N}=\text{B}=\text{N}]^{3-}$ units are showing significant deviations from linearity ($\angle\text{N-B-N} = 167\text{-}180^\circ$). The local arrangement around the dinitridoborate anions is usually 6 (trigonal prism or antiprism) but can be extended to 7 or 8, when larger cations are present. A careful glance on Table. 1 shows that most of the study done in this area has been focusing on dinitridoborate fluorides and chlorides in combination with Mg, Ca, Sr and Ba as counter ions. From the structural point of view, it is quite amazing, that there is no dinitridoborate halide known yet, in which both the spherical halides and the rod-like (BN_2) are coordinated by the same type of polyhedra. Another aspect worth mentioning is the missing of the chloride, bromide and iodide compounds of Eu in these series, despite the fact that crystal chemically related Sr compounds are well characterized. But unlike Sr, Eu can employ both the oxidation states +2 and +3 and hence, its insertion into the crystal structure might lead to novel phases with interesting physical properties in which Eu is mixed valent or in +3 state.

Several attempts have been made, yet, to use the rod-like $[\text{BN}_2]^{3-}$ units as a reactive precursor for synthesis of novel materials. They all failed due to the insolubility of the starting compounds in conventional aprotic solvents, even at elevated temperatures. Alternatively, a suitable salt melt - such as alkali and earth alkaline halides - could be an attractive system for the mobilization of the dinitridoborate anions for chemical and

electrochemical reactions. Li, Mg and Ca cations are known to act as catalyst in the complex polymerization processes taking place during conversion of h-BN to c-BN. Similar reactions can also be expected in salt melts yielding novel materials with 2D and 3D-(B-N) framework structures and unusual physical properties, such as hardness, chemical inertness and refractoriness.

In the present study the hitherto unknown EuN/EuX₂/BN (X = Br, I) system and the known but structurally not characterized phases M^{II}₂[BN₂]Br were investigated by means of phase, thermal and X-ray single crystal structure analyses, as well as via vibrational spectroscopy. The oxidation states of Eu were determined by magnetic measurements and EPR and Mössbauer spectroscopy.

Beside the “expected” phases with the well-known compositions M^{II}₂[BN₂]Br (M^{II} = Ca, Sr, Eu) and Eu₂[BN₂]I but new crystal structures, the present investigations led also to two novel compounds with tri- and mixed-valent Eu exhibiting interesting structural and magnetic properties.

In the following, we will report on the crystal structures and physical properties of the compound series M^{II}₂[BN₂]Br (M^{II} = Ca, Sr, Eu) and Eu₂[BN₂]I comprising isolated dinitridoborate units and the novel phases Eu^{III}₃[B₃N₆] and Li_{0.42}Eu^{II/III}₃[B₃N₆] with the cyclic moieties [B₃N₆]⁶⁻, isosteric to [B₃O₆]⁶⁻.

Chapter 2

EXPERIMENTAL METHODS

2.1 Introduction remarks

Due to the air and moisture sensitivity of products and educts, all manipulations, experimental preparations and storage were carried out in argon filled glove boxes. In addition to these, glass containers and preparatory apparatus were dried in a hot air sterilizer laboratory oven at 393 K for several hours before antechamber operation which was performed to transfer any container by either three rapid evacuations of at least two minutes each or one long evacuation of 30-60 minutes depending on the size of the material to be transferred. The conditions in the glove-box were controlled by monitoring the oxygen and water level in parts per million with the minimum threshold set at ≤ 0.1 ppm for O₂ and H₂O. Argon excess pressure was set at 2mbar.

2.2 Materials and Chemicals Used, Sources and Quality

All starting materials were highly pure chemicals either purchased from chemical companies or prepared in the laboratory. Table 2.1 gives an overview of the chemicals and elements including their sources and purity.

Elements/ Chemicals	Company	Physical State	Atomic Weight	Packaging	Quality Description
Nitrogen (N)	Messer- Ali Gaz	Colorless gas	14.01	Evaporated liquid nitrogen	99.999%
Lithium	TBL-Kelpin	Rods	6.941	Sealed under Ar in metal can	3N
Europium	MPI-CPFS	Crystalline dendritic pieces	151.96	Sealed under Ar in quartz glass tube	99.95%
Calcium	Alfa-Aeasar	Crystalline dendritic pieces	40.10	Sealed under Ar in quartz ampoule	99.98%
Strontium	Alfa-Aeasar	Crystalline dendritic pieces	87.62	Sealed under Ar in quartz ampoule	99.98%
Boron Nitride	Alfa-Aeasar	Anhydrous Powder	24.81	Sealed under Ar in quartz ampoule	99.98%
Europium (III) Chloride	Sigma - Aldrich	Anhydrous Powder	258.32	Sealed under Ar in quartz ampoule	99.99%
Europium (II) Bromide	Sigma - Aldrich	Anhydrous Powder	311.72	Sealed under Ar in quartz ampoule	99.99%
Europium (II) Iodide	Sigma - Aldrich	Anhydrous Powder	405.77	Sealed under Ar in quartz ampoule	99.99%
Nb-crucible	Plansee (Austria)	Metallic crucibles		Crucible	99.9%
Nb-tube	Plansee	Shinning silver tube		20 cm tube 8 mm Ø	99.9%

Table 2.1 Chemicals and Elements

For the preparation of binary nitrides, Lithium, Calcium, Strontium and Europium metals were used as pieces cut from rod or dendritic pieces respectively, which were placed inside a Niobium crucible and kept under ambient back pressure of nitrogen at 1023 K for 12

hours inside a typical quartz glass tube reactor as shown in Fig 2.1. The purity of the products was checked by powder x-ray diffraction measurements and elemental analysis. In order to keep the number of impurity elements at its lowest, all the binaries used as starting material, were synthesized using exclusively Niobium crucibles. No traces of the crucible materials were detected in the reaction products.

2.3 Experimental Methods

2.3.1 Gas Purification System and Glove Box

Most nitrides are synthetically challenging, thus requiring specialized techniques, maneuverings and reliable inert atmosphere for the preparation. In our laboratories, MBRAUN gas purification system is used together with a glove box for the enabling and maintaining a pure inert gas atmosphere inside a hermetically sealed enclosure (Figure 2.1). Standard MBRAUN glove box is filled with inert gas (Argon) and the pressure is automatically regulated at 1 atm. The argon is circulated continuously through gas purification system to keep the O_2 and H_2O levels lower than 1 ppm.[26]

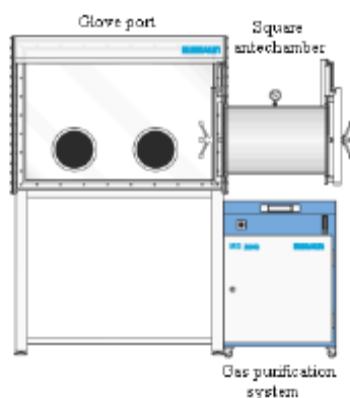


Figure 2.1 MBraun Gas Purification and Glove Box[MBraun].

2.3.2 High Temperature Annealing in Quartz Tube and Sealed Ampoules

Quartz glass tube (diameter of 40mm, a length of 500 mm, a wall thickness of 1.5 mm), Duran glass mouth- cap with valves stoppers and Niobium crucibles (\varnothing about 8 mm in length from 20 to 25 mm) were used for the preparation of binary nitrides. Before every reaction, the sealants were used between the glass joints due to circulation process and high temperatures. After Niobium crucible was filled with starting materials, it was put in to the reactor tube. The reactor was evacuated with a vacuum pump until the pressure reached 1×10^{-3} pa then constant N_2 flow was adjusted with a bubbler in the exhaust of reactor to one bubble per second for nitrogen back pressure.

The furnaces used for the reactions with the quartz glass tube reactor had the furnace standby temperature of 323K, and the reactions were cooled down to 323K after the heat treatment. After the reaction, the reactors were taken out and with slight reaction pressure inside. They were transferred into the glove box after pre – evacuating the quartz glass tube before placing into the antechamber.

For the synthesis of ternary nitride-borates, the binaries were mixed and filled into the Niobium tubes that were then arc-welded under argon at a pressure of 400 mbar to form an ampoule. To protect against oxidation, the ampoules were encapsulated in a quartz ampoule under argon atmosphere. The reactions were held in box furnaces (Nabertherm) which can be programmed within temperature range 20 – 1100 C. After the reaction, the ampoules were opened and manipulated for further investigations inside the glove-box.

2.4 Materials Characterization

2.4.1 X-Ray Diffraction Techniques

X-ray powder diffraction technique was used as one of the primary tools for the characterization of reaction products and educts. It was also used to assign the purity of the product. The experimentally obtained powder patterns were compared with the ones in

databases like Inorganic Crystal Structure Database (ICSD) [27] and Search/Match program in Stoe WinXPOW software [28]. The experimental powder diffractograms were also compared with those calculated from the Rietveld and single crystal structure refinements. In addition to these, the structural characterization of microcrystalline materials that are unsuitable for investigation by single-crystal diffraction techniques due to crystal twinning, other types of defects, lack of appropriate size and quality, etc. [29] was also investigated by X-Ray powder diffraction techniques. Internal standard (LaB_6) was used for the accurate lattice parameters and structure determination of a crystalline sample.

Since products and educts are air and moisture sensitive, the samples were finely ground and sandwiched between two Polyimide (Kapton) films by using special aluminum sample holders in a nitrogen filled glove- box (O_2 and $\text{H}_2\text{O} \leq 1$ ppm). For the probe preparation, the first film was placed on the aluminum sample holder and few drops of Vaseline in hexane solution was added and waited for evaporation of hexane. The powder sample was spreaded and a thick layer of silicon fat was smeared on the periphery of the first film for air tight sealing. Then the second protecting film was placed on top of the first film and fixed by a second aluminum o ring.

X-ray powder diffraction analysis was performed by using Huber G670 equipped with a germanium monochromator and $\text{CuK}_{\alpha 1}$ radiation. Data collections were made in the range of $3^\circ \leq 2\theta \leq 100^\circ$ range with a step size of $0.005^\circ 2\theta$. After data collection, Stoe WinXPOW software package [27] was used in the analysis of X-ray powder diagrams and WinCSD Cell program was used for refinement of the unit cell parameters by using LaB_6 as internal standard.

Suitably sized crystal with well-formed edges and faces were picked and sealed inside a glass capillary for the single crystal measurements. The single crystal data were collected at room temperature on a Rigaku AFC7 four circle diffractometer equipped with a Mercury-CCD detector (MoK_{α} radiation, graphite monochromator). After data collection

the structures was solved by direct methods, using SHELXS-97 [30] and refined by using the full-matrix least-squares procedure SHELXL-97 [31].



Figure 2.2 X-ray sample holder and Polyimide (Kapton[®]) film for moisture sensitive samples

2.4.2 Differential Thermal Analysis (DTA)

Differential Thermal Analysis was used for the investigation of phase transitions and optimization of the reaction parameters. In DTA, The sample and reference chambers are equally heated according to a temperature regime in which a transformation takes place within the sample. As the sample temperature infinitesimally deviates from the reference temperature, the device detects it and reduces the heat input to one cell while adding heat to the other, so as to maintain a zero temperature difference between the sample and reference, establishing a null balance. The quantity of electrical energy per unit time which must be supplied to the heating elements, in order to maintain this null balance, is assumed to be proportional to the heat released per unit time (Watts) by the sample.[32]

DTA measurements were done with NETZSCH DTA 404 which was integrated inside an Ar filled glove box. The air sensitive measurements were performed using Nb ampoules which were sealed after filling approximately 30 mg sample in an argon-filled glove box. The measurements were carried out by applying a heating and cooling rate of 10 K /min with Ar flow up to 1600 K. Once the final temperature of the heating cycle was

reached, the cooling was immediately begun without further preservation time at that temperature. Data manipulation and analysis were performed with the software program called NETZSCH (NETZSCH Proteus – Thermal Analysis-Version 4.0 beta and 4.3, NETZSCH-Geraetebau GmbH 1999). After the measurements, X-ray powder diffraction analysis was applied to the samples in order to determine the type of products formed during the heat treatment.

2.4.3 Infrared Spectroscopy

Infrared Spectroscopy was used to investigate on excitation of the bonds inside the molecular groups by electromagnetic radiation in the IR-range. The dipole moment of the molecule is changed through excitation and the specific vibrational frequencies at which the isolated molecular groups vibrates were identified through analysis of the absorption bands [33].

For the measurement, the specimens were prepared by mixing finely ground 4 mg of compound with 400 mg of dried potassium bromide and pressing in an evacuated die under 8 tons of pressure for 5 minutes to make a pellet of 13 mm diameter. Due to the air and moisture sensitivity of compounds, the pellets were prepared in a nitrogen filled glove-box (O_2 and $H_2O \leq 1$ ppm). and transferred to FT-IR device which was running under vacuum to avoid the presence of water and CO_2 bands in the resulting spectrum. The Spectra were recorded from KBr pellets by using JASCO FT-IR 600 Spectrometer in the range of $4000 - 400 \text{ cm}^{-1}$ and data manipulations were done by using JASCO Spectra Manager Software [34].



Figure 2.3 Setup for preparing 13mm pellet for IR measurement

2.4.4 Raman Spectroscopy

Raman Spectroscopy was used to study vibrational, rotational and other low-frequency modes in isolated molecular moieties which are originating from inelastic scattering, or so called Raman scattering of monochromatic light from a laser in the visible, near IR or near UV range [35].

The FT-Raman spectra were recorded on polycrystalline samples with a Bruker RFS 100/S spectrometer (Nd: YAG-Laser, 1064 nm, 200 mW) which were filled to a Pyrex tubes ($\varnothing = 4$ mm) in nitrogen filled glove- box (O_2 and $H_2O \leq 1$ ppm) and sealed by using a propane gas torch. Data manipulations were done by using OPUSTM software [36]

2.4.5 ESR Spectroscopy

ESR spectroscopy was studied for determination of the valance state of Eu ions and the possibility of vacant Li-sites. The ESR spectra were recorded from powder samples with Bruker Elexys E500, X-Band ESR (9.4 GHz) in a temperature range from 5-300K. The powder samples were mixed with dry paraffin and filled inside a suprasil quartz glass electron paramagnetic resonance spectroscopy cell in nitrogen filled glove- box (O_2 and

$\text{H}_2\text{O} \leq 1$ ppm). Then the sample was sealed under slightly reduced pressure (400mbar) of helium gas.

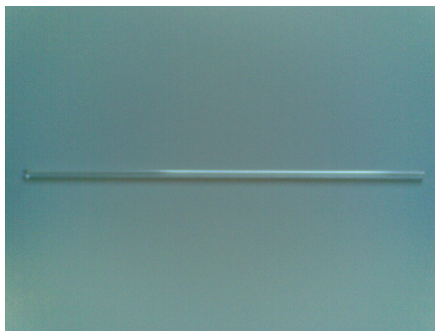


Figure 2.4 Calibrated thin walled quartz tube for ESR measurement

2.4.6 Eu^{151} Mössbauer Spectroscopy

Mössbauer Spectroscopy was used to study the valance state of Eu ions by determining the isomer shifts occurring from the non-zero volume of the nucleus and the electron charge density due to s-electrons. Any difference in the s-electron environment between the source and absorber produces a shift in the resonance energy of the transition. This transition shifts the whole spectrum positively or negatively depending on the s-electron density, and sets the centroid of the spectrum.[37]

The 21.53 keV transition of ^{151}Eu with an activity of 130 MBq (2% of the total activity of a $^{151}\text{Sm}:\text{EuF}_3$ source) was used for the Mössbauer spectroscopic experiment which was conducted in the usual transmission geometry. The measurement was performed with a commercial helium bath cryostat. The temperature of the absorber was kept at 78 K, while the source was kept at room temperature. The sample was placed within a thin-walled glass container sealed with an ultra-violet glue. The thickness of the sample corresponded to about 10 mg Eu/cm^2 .

2.4.7 Magnetic Susceptibility Measurements

Magnetic susceptibility measurements were done to determine the ratio magnetization of the samples in an applied magnetic field. The magnetic susceptibility of the samples was extracted by taking the linear slope of the inverse magnetic susceptibility with respect to temperature by applying the Curie – Weiss law.

The magnetic susceptibility measurements were carried out in a Superconducting Quantum Interface Device (SQUID) magnetometer (MPMS XL – 7, Quantum Design). Since the samples for the measurement are air and moisture sensitive compounds, the sample (≈ 100 mg) were sealed inside pre – calibrated thin walled quartz tubes (wall thickness = 1mm) under a He – pressure of 400mbar (Figure 2.6). The magnetic susceptibilities were measured in the temperature range 1.8 K – 300 K with a fixed magnetic field from 20 Oe to 70 kOe.

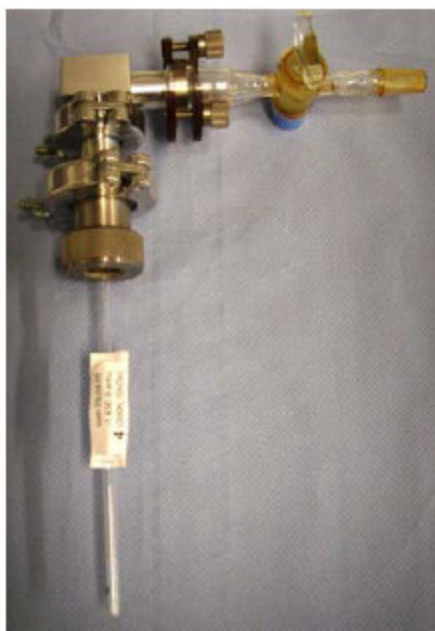


Figure 2.5 Calibrated thin walled quartz tube for magnetic susceptibility measurement

Chapter 3

$M^{II}_2[BN_2]Br$ ($M^{II} = Ca, Sr, Eu$)

3.1 Synthesis

Due to the air and moisture sensitivity of products and educts, all manipulations - such as grinding, weighing and sample preparations for measurements - as well as the storage of the reactants and the products were carried out in a nitrogen filled glove- box (O_2 and $H_2O \leq 1$ ppm).

The title compounds $M^{II}_2[BN_2]Br$ ($M^{II} = Ca, Sr, Eu$) were synthesized from the mixture of the binaries Ca_3N_2 (Sr_2N, EuN), h-BN and MBr_2 . For the preparation of $Ca_2[BN_2]Br$, a molar ratio of 1: 1:1,1 and for $Sr_2[BN_2]Br$ a slight excess of Sr_2N were employed (1,5 : 1:1,1). and for $Eu_2[BN_2]Br$, a molar ratio of 2:1:1,1 ($\Sigma m = 400$ mg). The educts were ground until a fine homogeneous powder was obtained. The mixture was transferred into a clean niobium ampoule, arc-welded and sealed in an evacuated silica tube. To optimize the reaction parameters, the specimens were thermally investigated by DTA (Fig 3.4.1 and Fig 3.4.3). The reaction ampoule was then placed in a muffle furnace and heated up to 1273 K for $Ca_2[BN_2]Br$ and 1023 K for $Sr_2[BN_2]Br$ and $Eu_2[BN_2]Br$ within 8 hours. After 24 hours of annealing, the samples were cooled down to room temperature during 8 hours.

$Ca_2[BN_2]Br$ and $Sr_2[BN_2]Br$ were obtained as white to pale yellow microcrystalline powders while $Eu_2[BN_2]Br$ forms orange thick crystals and pale yellow thin plate-like crystals. All three compounds are sensitive to air and moisture. The purity of the samples was verified using X-ray powder diffraction method. Fig 3.1.1, Fig 3.1.2 and Fig 3.1.3 show the comparison of the observed powder diffractograms of $Ca_2[BN_2]Br$, $Sr_2[BN_2]Br$

and $Eu_2[BN_2]Br$ with those calculated from Rietveld and single crystal data. The presence of only few foreign reflections in the diagrams and the good match of the both theoretical and experimental patterns proved that the nitridoborate halide samples were highly pure.

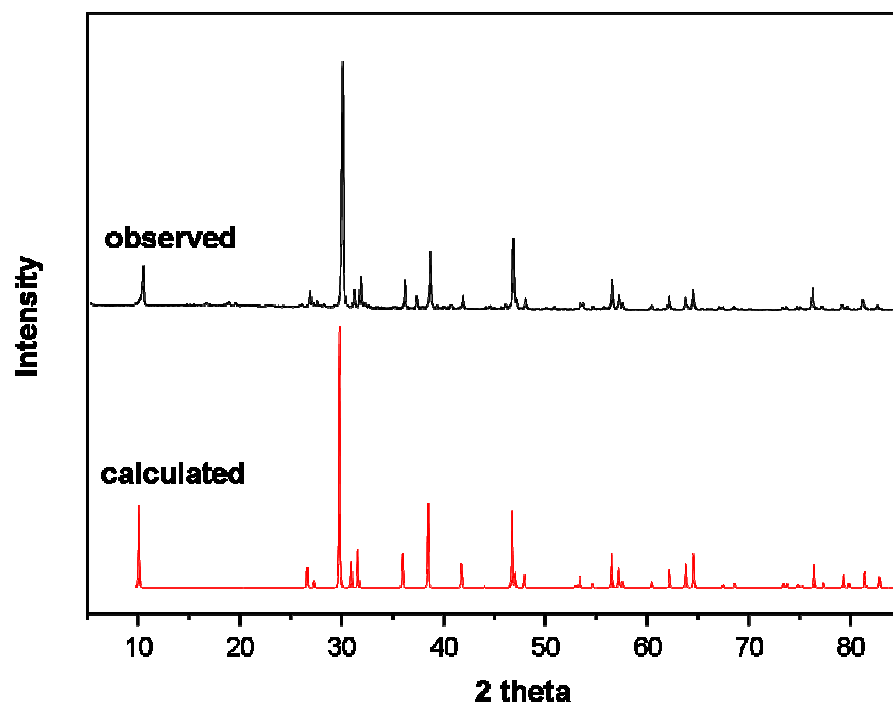


Fig 3.1. 1 Observed and calculated X-ray Powder diffraction patterns of $Ca_2[BN_2]Br$

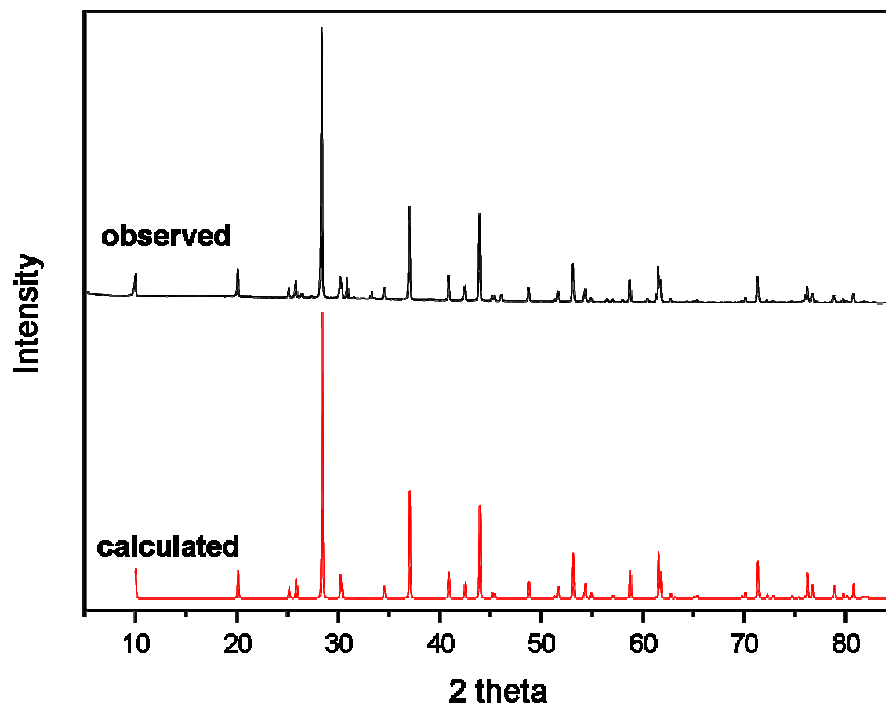


Fig 3.1. 2 Observed and calculated X-ray Powder diffraction patterns of $Sr_2[BN_2]Br$

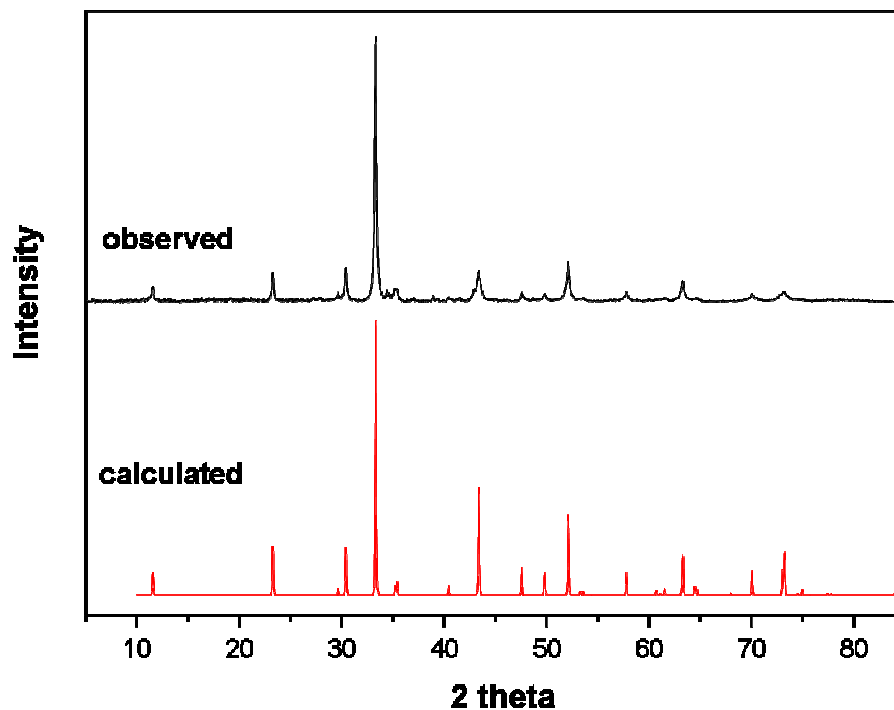


Fig 3.1.3 Observed and calculated X-ray Powder diffraction patterns of $Eu_2[BN_2]Br$

3.2 Crystal Structure

Due to the lack of suitable single crystals, the crystal structure of both $Ca_2[BN_2]Br$ and $Sr_2[BN_2]Br$ were solved from powder data using Rietveld methods. The X-ray diffraction pattern was obtained on a Imaging Plate Guinier Diffractometer 670 using $CuK\alpha_1$ radiation. The Rietveld refinements were performed with the program WinCSD [38]. The structure models were drawn by using the program DIAMOND 3 [39]. The crystal structure of $Eu_2[BN_2]Br$ was determined by single-crystal X-ray diffraction methods. The single crystal data were collected at room temperature on a Rigaku AFC7 four circle diffractometer equipped with a Mercury-CCD detector ($MoK\alpha$ radiation, graphite monochromator). After data collection the structures was solved by direct

methods, using SHELXS-97 [29] and refined by using the full-matrix least-squares procedure SHELXL-97 [31].

The isotopic compounds crystallize in the space group $R\bar{3}m$ (Pearson code hR6; $Z = 3$) with $a = 3.86897(7)\text{\AA}$, $c = 25.8135(6)\text{\AA}$ for $Ca_2[BN_2]Br$, $a = 4.11681(3)\text{\AA}$, $c = 26.4606(2)$ for $Sr_2[BN_2]Br$ and $a = 4.0728(3)\text{\AA}$, $c = 26.589(2)\text{\AA}$ for $Eu_2[BN_2]Br$. The crystal structures are isotopic to $Sr_2[CuO_2]Br$ and can be interpreted as a substitution variant of anti- $NaFeO_2$ type of structure with M and Br at Na and Fe positions, respectively. The structure is characterized by layers of edge-sharing $[N-B-N]@M^{II}_6$ and $[Br]@M^{II}_6$ trigonal antiprisms ($M = Ca, Sr, Eu$) which are alternately stacked along $[001]$. The bond lengths for the strictly linear $[BN_2]^{3-}$ anions are $d(B-N) = 1.353(7)\text{\AA}$ ($M = Ca$), $1.355(4)\text{\AA}$ (Sr) and $d(B-N) = 1.355(8)\text{\AA}$ (Eu) harmonizing well with those of the well-known dinitrido borates [40]

During the single crystal investigation on $Eu_2[BN_2]Br$, the structure refinement was first performed with full occupancy factors for all atoms and resulted in $R = 0.033$ and $wR2 = 0.078$ but atomic displacement parameters for boron position were too small which was interpreted as indication for presence of a strong scattering in this site. After realizing of ADP and site occupancies for boron positions, $R = 0.032$; $wR2 = 0.075$ with displacement values of $0.010(4)$ and $0.011(2)$ and SOF of $1.50(2)$ and $0.90(4)$ was obtained for B and N, respectively. This result shows that there is a partial substitution of $[N-B-N]^{3-}$ and $[Br]^-$ anions and can be easily explained because of the similar cationic environments. After B position was constrained to be mixed occupied by boron and bromine atoms in the separate refinement, the degree of disorder was determined as $4(1)\%$.

The crystal data and the conditions for data collection and refinement for $M^{II}_2[BN_2]Br$ ($M^{II} = Ca, Sr, Eu$) are summarized in Table 3.1.1 and Tables 3.1.2, 3.1.3, 3.1.4 contain the atomic coordinates and displacement parameters and Table 3.1.5, 3.1.6 and 3.1.7 depicts the important bond lengths and bond angles.

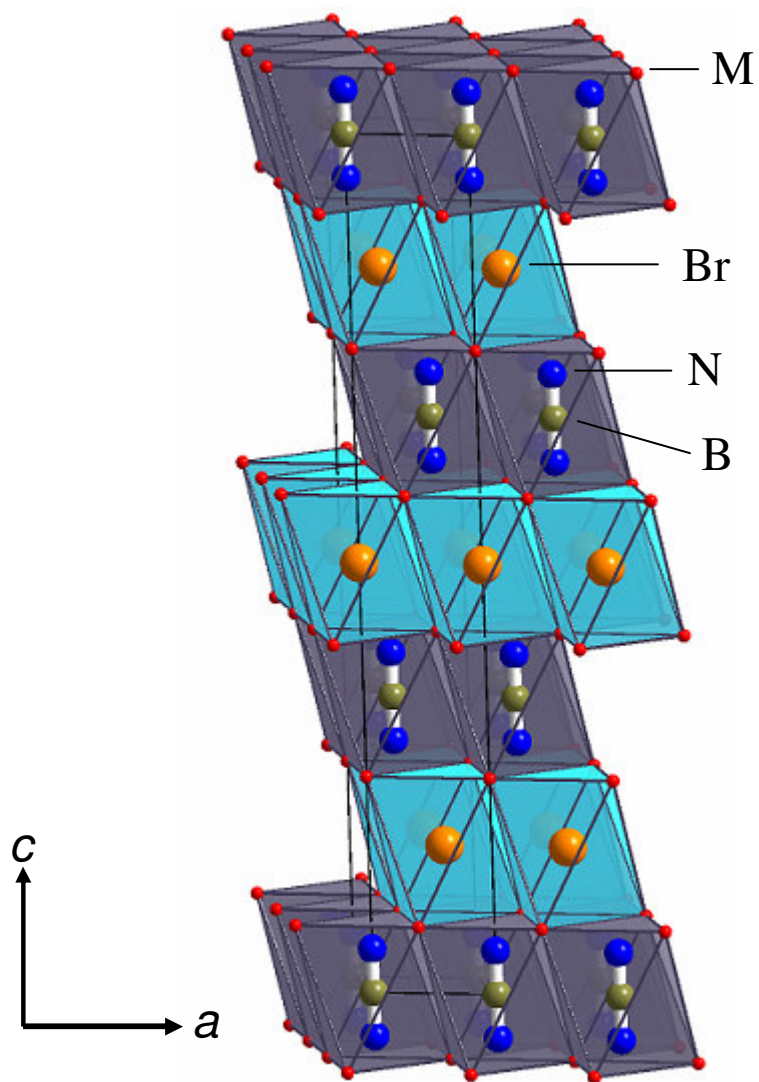


Fig 3.2 1 The crystal structure of $M^{II}_2[BN_2]Br$ ($M^{II} = Ca, Sr, Eu$)

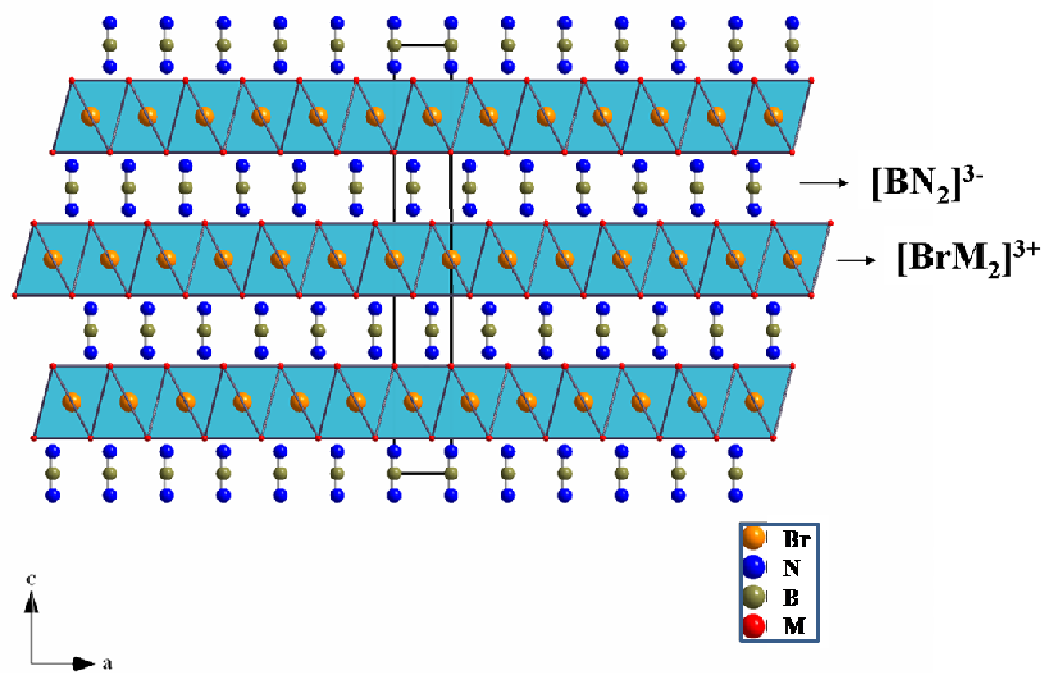


Fig 3.2 2 The crystal structure of $M^{II}_2[BN_2]Br$

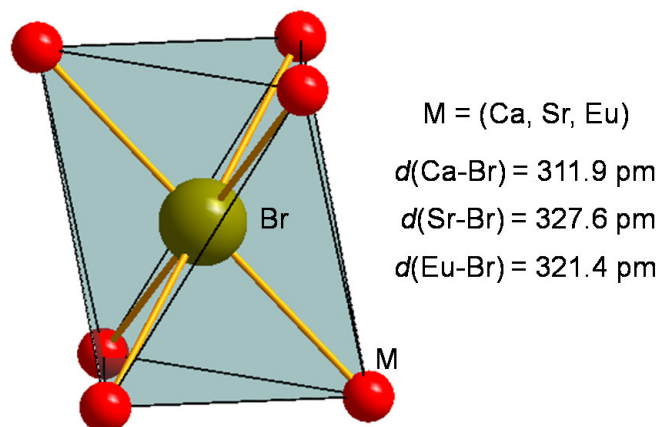


Fig 3.2 3 Trigonal anti prismatic coordination of M around Br atoms in the crystal structures of $M^{II}_2[BN_2]Br$ ($M^{II} = Ca, Sr, Eu$).

Compound	$Ca_2[BN_2]Br$	$Sr_2[BN_2]Br$	$Eu_2[BN_2]Br$
Crystal system	trigonal rhombohedral	trigonal rhombohedral	trigonal rhombohedral
Crystal color, shape, size	white microcrystalline powder	white microcrystalline powder	Pale yellow plate
Space group	$R\bar{3}m$ (No. 158)	$R\bar{3}m$ (No. 158)	$R\bar{3}m$ (No. 158)
Z	3	3	3
a [\AA]	3.86897(7)	4.11681(3)	4.0728(3)
b [\AA]	3.86897(7)	4.11681(3)	4.0728(3)
c [\AA]	25.8135(6)	26.4606(2)	26.589(2)
V [\AA^3]	334.63(2)	388.38(9)	381.96(2)
d_x [$\text{g}\cdot\text{cm}^{-3}$]	8.56	12.56	5.512
Diffractometer	Huber G670	Huber G670	Rigaku AFC 7
Detector	Image Plate	Image Plate	Mercury CCD
Monochromator	Germanium	Germanium	Graphite
Radiation, Wavelength	Cu $K_{\alpha 1}$, 1.540598	Cu $K_{\alpha 1}$, 1.540598	Mo K_{α} , 0.71073
Scan mode	2 θ	2 θ	ϕ/φ
2 θ range [$^\circ$]	6.03, 85;	6.03, 100;	9.20, 62.96

	0.005	0.005	
No. Refl.			
No. Refl. unique			203
R_{int}			0.0413
Structure solution method	Rietveld	Rietveld	Direct Methods
Program for structure solution	WinCSD[38]	WinCSD[38]	SHELXS-97[30]
Program for structure refin.	GSAS[10]	GSAS[10]	SHELXL-97[31]
Refined parameters	11	11	9
Goof			1.225
R_1, wR_2 (all data)			0.0327, 0.0774
R_{prof}, R_{int}	0.1760, 0.0824	0.1093, 0.348	

Table 3. 1 Crystallographic data and refinement details for $M_2[BN_2]Br$ ($M = Ca, Sr, Eu$).

Atom	Site	X	Y	z	U_{iso} / U_{eq}
Br	3a	0	0	0	0.0228(8)
Ca	6c	0	0	0.2489(7)	0.0253(11)
N	6c	0	0	0.4476(3)	0.0290(2)
B	3b	0	0	½	0.0084(2)

Table 3. 2 Atomic coordinates and displacement parameters [in \AA^2] for $Ca_2[BN_2]Br$. Standard deviations are given in parentheses

Atom	U_{11}	U_{22}	U_{33}	U_{12}	U_{13}	U_{23}
Ca1	0.024(1)	0.024(1)	0.025(2)	0.0107(6)	0	0
Br1	0.0210(8)	0.0210(8)	0.021(2)	0.0063(4)	0	0

Table 3.3 Anisotropic displacement parameters [10^{-4} pm^2] for $Ca_2[BN_2]Br$, standard deviations of the last digit in parentheses

Atom	Site	X	Y	z	U_{iso} / U_{eq}
Br	3a	0	0	0	0.0220(4)
Sr	6c	0	0	0.24812(2)	0.0160(3)
N	6c	0	0	0.44880(2)	0.021(1)
B	3b	0	0	1/2	0.009(4)

Table 3.4 Atomic coordinates and displacement parameters [in \AA^2] for $Sr_2[BN_2]Br$. Standard deviations are given in parentheses.

Atom	U_{11}	U_{22}	U_{33}	U_{12}	U_{13}	U_{23}
Sr1	0.0137(3)	0.0137(3)	0.0207(6)	0.0068(2)	0	0
Br1	0.0193(5)	0.0193(5)	0.0274(9)	0.0097(2)	0	0

Table 3.5 Anisotropic displacement parameters [10^{-4} pm^2] for $Sr_2[BN_2]Br$, standard deviations of the last digit in parentheses

Atom	Site	x	Y	z	U_{iso} / U_{eq}	Occupancy
Br1	3a	0	0	0	0.0172(4)	1
Br2	3b*	0	0	1/2	0.010	0.046(8)
Eu	6c	0	0	0.249073(17)	0.0142 (3)	1
N	6c	0	0	0.4491(3)	0.011	0.954(8)
B	3b*	0	0	1/2	0.010	0.954(8)

Table 3.6 Atomic coordinates and displacement parameters [in \AA^2] for $Eu_2[BN_2]Br$. Standard deviations are given in parentheses.

Atom	U_{11}	U_{22}	U_{33}	U_{12}	U_{13}	U_{23}
Eu1	0.0110(4)	0.0110(4)	0.0207(4)	0.0055(2)	0	0
Br1	0.0166(4)	0.0166(4)	0.0185(7)	0.0083(2)	0	0

Table 3.7 Anisotropic displacement parameters [10^{-4} pm^2] for $Eu_2[BN_2]Br$, standard deviations of the last digit in parentheses

Atom 1	Atom 2	d1,2[Å]	n	Atom 1	Atom 2	d1,2[Å]	n
Br-	Ca	3.119(1)	6x	N-	B	1.353(7)	1x
					Ca	2.364(2)	3x
Ca-	N	2.364(2)	3x	B-	N	1.353(7)	2x
	Br	3.119(1)	3x		Ca	3.083(1)	6x
	B	3.083(1)	6x				
		$\angle(N-B-N)$	180°				

Table 3.8 Selected atomic distances [Å] and bond angles [°] in $Ca_2[BN_2]Br$ with their multiplicity (n). Standard deviations are given in parentheses

Atom 1	Atom 2	d1,2[Å]	n	Atom 1	Atom 2	d1,2[Å]	n
Br-	Sr	3.2762(4)	6x	N-	B	1.355(4)	1x
					Sr	2.508(1)	3x
Sr-	N	2.508(1)	3x	B-	N	1.355(4)	2x
	Br	3.2762(4)	3x		Sr	3.2085(4)	6x
	B	3.2085(4)					
		$\angle(N-B-N)$	180°				

Table 3.9 Selected atomic distances [Å] and bond angles [°] in $Sr_2[BN_2]Br$ with their multiplicity (n). Standard deviations are given in parentheses

Atom 1	Atom 2	d1,2[Å]	n	Atom 1	Atom 2	d1,2[Å]	n
Br2-	Eu	3.2141(3)	6x	N-	B	1.354(8)	1x
Br1-	Eu	3.2479(3)			Eu	2.496(3)	3x
Eu-	N	2.496(3)	3x	B-	N	1.354(8)	2x
	Br2	3.2141(3)	3x		Eu	3.2141(3)	6x
	Br1	3.2479(3)					
		$\angle(N-B-N)$	180°				

Table 3.10 Selected atomic distances [Å] and bond angles [°] in $Eu_2[BN_2]Br$ with their multiplicity (n). Standard deviations are given in parentheses

3.3 Physical Properties

3.3.1 Infra-Red and Raman Spectroscopy

The vibrational spectra of the $Ca_2[BN_2]Br$, $Sr_2[BN_2]Br$ and $Eu_2[BN_2]Br$ compounds are characterized by the linear $[BN_2]^{3-}$ moieties with the idealized symmetry $D_{\infty h}$ for which the following four fundamentals are expected:

$$\Gamma_{\text{vib}} = \nu_1(\Sigma_g)(R) + \nu_2(\Sigma_u)(IR) + \nu_3(\Pi_u)(IR).$$

The existence of the symmetry center applies for the mutual exclusion, so that $\nu_1(\Sigma_g)$ will be observed solely in Raman spectrum while $\nu_2(\Sigma_u)$ and double-degenerate $\nu_3(\Pi_u)$ appear exclusively in IR.

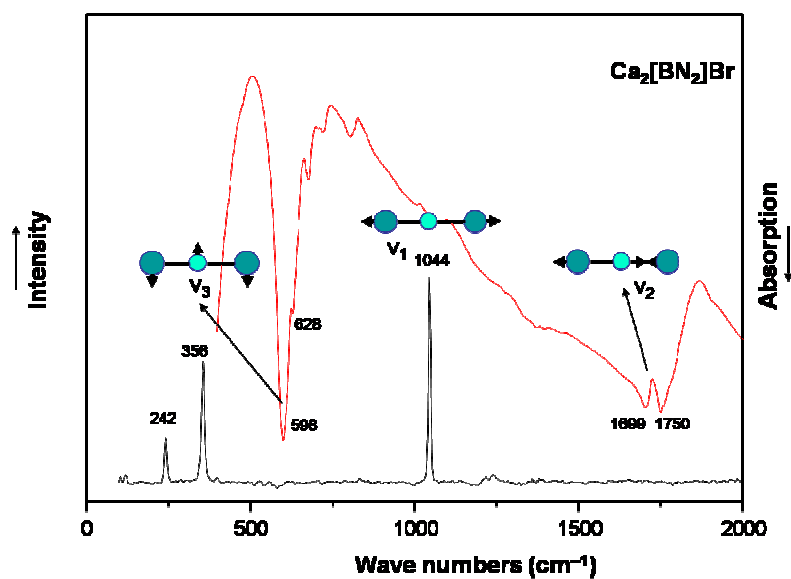


Fig 3.3 1 Vibrational Spectra of $Ca_2[BN_2]Br$. A = Absorption and I = Intensity, both in arbitrary units.

The vibrational spectra of the isostructural $M^{II}_2[BN_2]Br$ ($M^{II} = Ca, Sr, Eu$) are very simple showing only the expected $^{10}B / ^{11}B$ isotope splitting (Fig. 3.3.1). The symmetric and the antisymmetric (B–N) stretches are observed as intense bands at $\nu_1 = 1044 \text{ cm}^{-1}$ and

$\nu_2(^{11}B/^{10}B) = 1699 / 1750 \text{ cm}^{-1}$ ($M = Ca$), $\nu_1 = 1032 \text{ cm}^{-1}$ (RE), $\nu_2(^{11}B/^{10}B) = 1679 / 1732 \text{ cm}^{-1}$ (Sr) and $\nu_1 = 1028 \text{ cm}^{-1}$, $\nu_2(^{11}B/^{10}B) = 1671 / 1731 \text{ cm}^{-1}$ (Eu), respectively. The double degenerate deformation mode appears at $\nu_3(^{11}B/^{10}B) = 598 / 628 \text{ cm}^{-1}$ (Ca), $599 / 622 \text{ cm}^{-1}$ (Sr) and $587 / 612 \text{ cm}^{-1}$ (Eu).

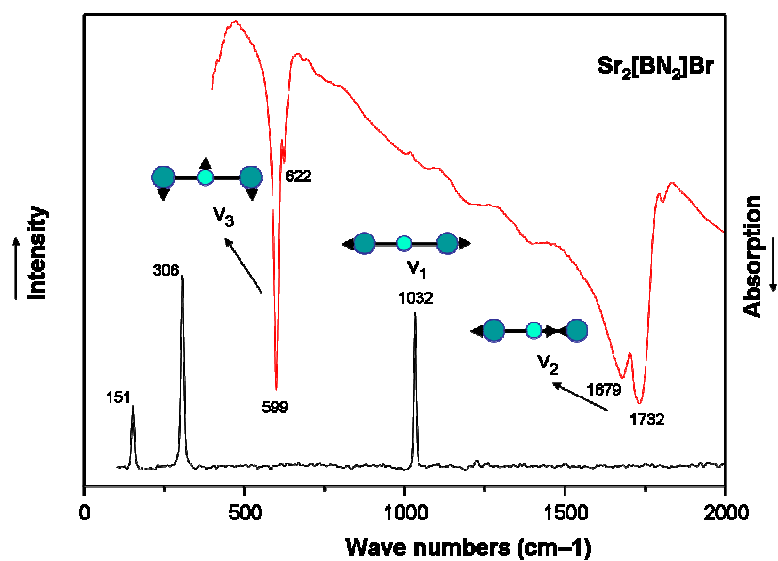


Fig 3.3 2 Vibrational Spectra of $Sr_2[BN_2]Br$. A = Absorption and I = Intensity, both in arbitrary units

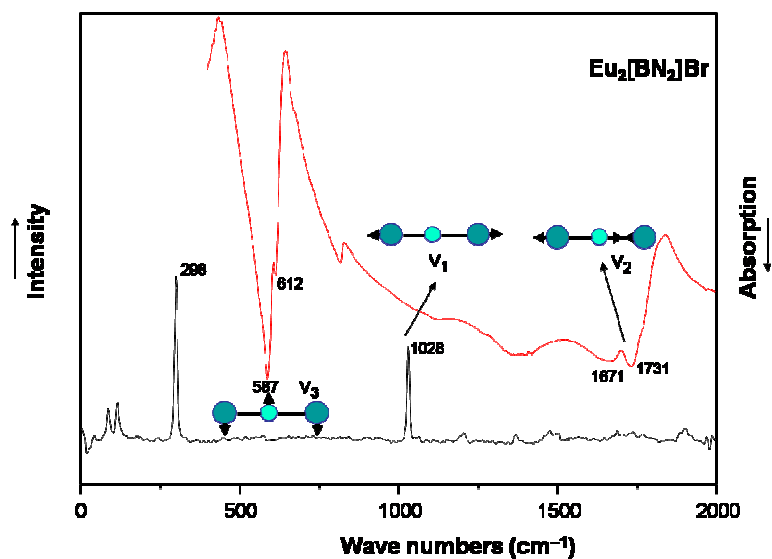


Fig 3.3.3 Vibrational Spectra of $Eu_2[BN_2]Br$. A = Absorption and I = Intensity, both in arbitrary units.

3.3.2 Differential Thermal Analysis

The ideal reaction temperature and possible phase transitions for $M_2[BN_2]Br$ ($M = Ca, Sr$) were investigated by Differential Thermal Analysis (DTA). The measurements were performed in the temperature range between 300K and 1573K with heating and cooling rates of 10K/min under flowing nitrogen gas stream and using arc-welded niobium crucibles. After the measurements, the heated samples were investigated by X-ray Powder diffraction method for further analyses.

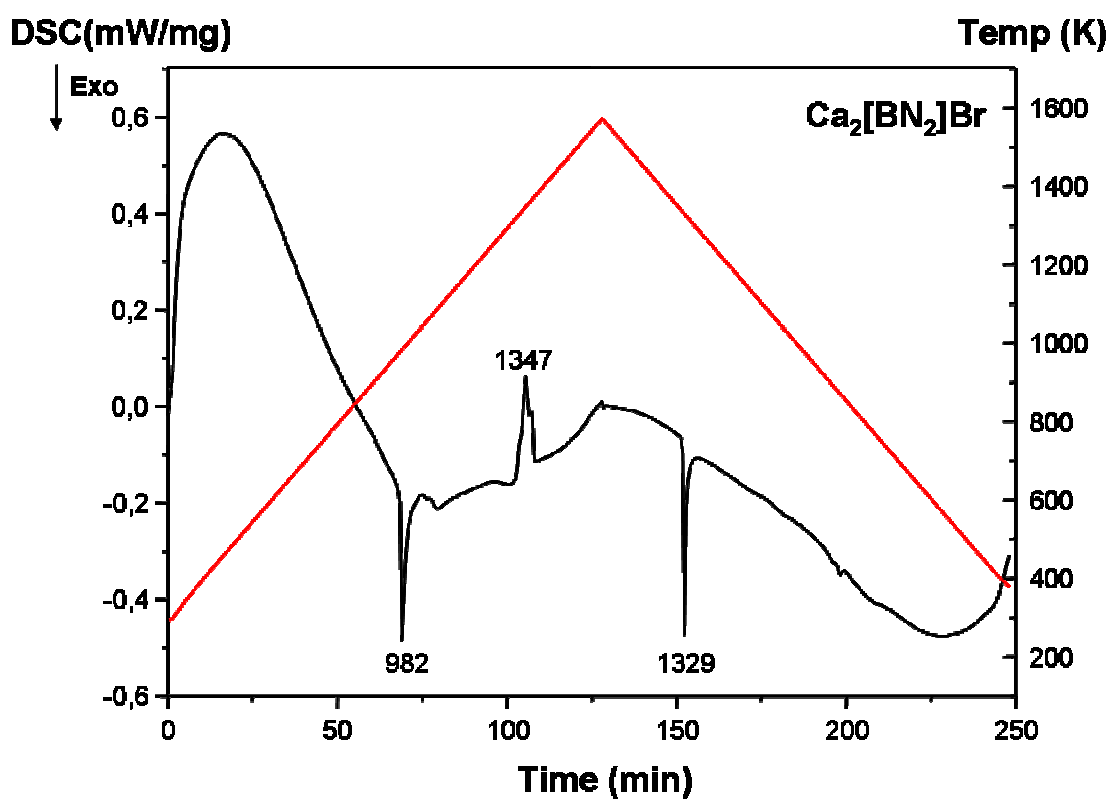


Fig 3.3 4 Differential Thermal Analysis curve of the starting mixtures for $Ca_2[BN_2]Br$, heated up to 1600 K. The Temperature of Exothermic and Endothermic peaks are labeled.

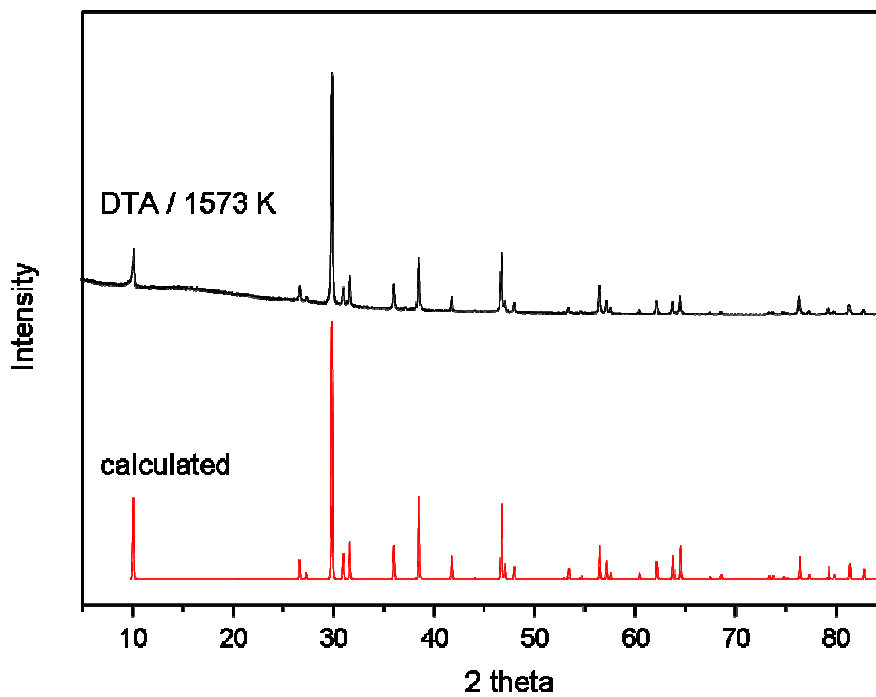


Fig 3.3 5 Powder X-ray diffraction pattern of DTA sample of $Ca_2[BN_2]Br$ after cooling from 1573 K showing the product is single phase $Ca_2[BN_2]Br$.

The formation steps of $Ca_2[BN_2]Br$ was followed up to 1573 K by Difference thermal analysis (Fig 3.3.4 showing sharp exothermic and endothermic effects at 982K and 1347K, respectively). The two peaks are indicating the reaction temperature and the melting point of the product. During the cooling step, sharp exothermic peak at 1329 K was observed and presumed to be the crystallization from the melt. Powder X-ray diffraction measurement of DTA sample (fig 3.3.5) revealed that the product of DTA measurement is pure $Ca_2[BN_2]Br$. From DTA results, the ideal reaction temperature was determined as 1273 K which is clearly below the melting point of $Ca_2[BN_2]Br$.

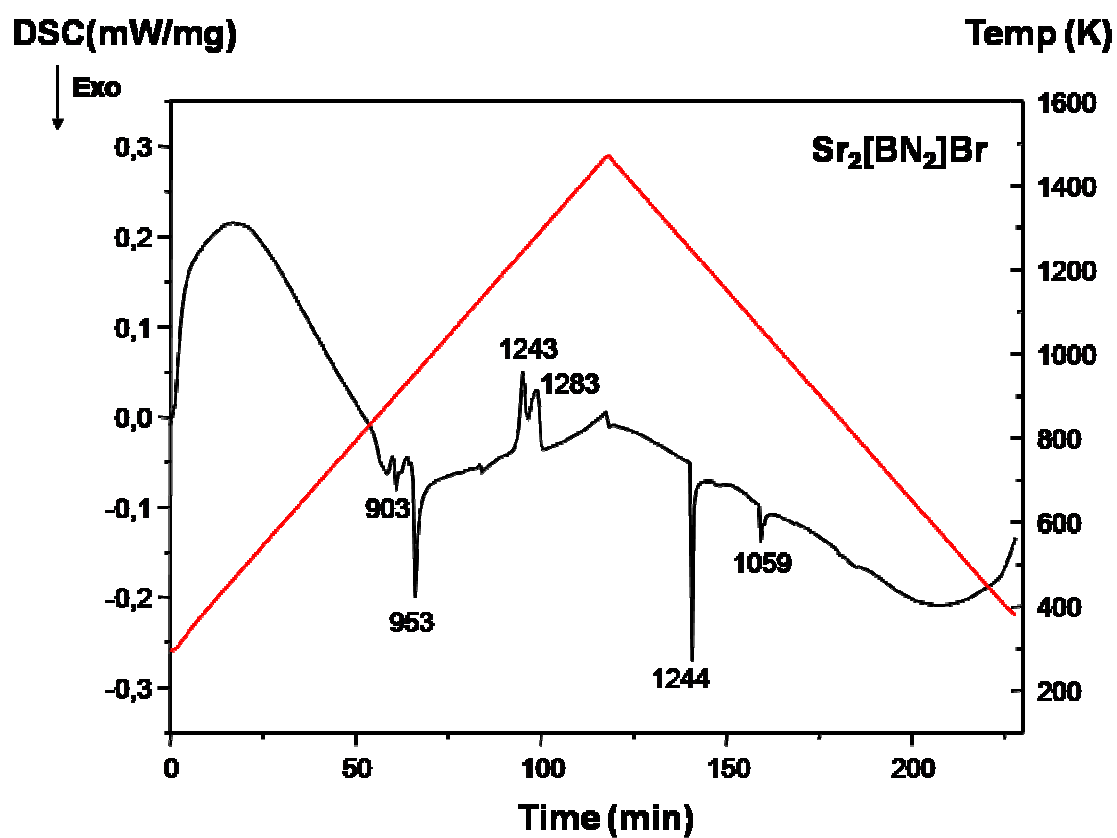


Fig 3.3 6 Differential Thermal Analysis curve of the starting mixtures for $Sr_2[BN_2]Br$, heated up to 1600 K. The peaks for exothermic and endothermic thermal effects are labeled.

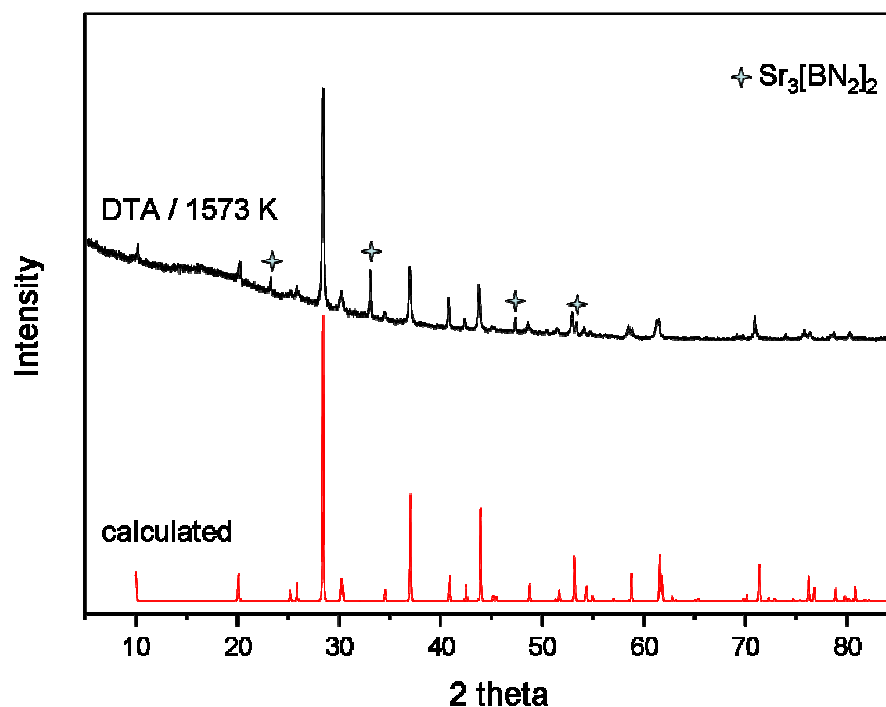


Fig 3.3 7 Powder X-ray diffraction pattern of DTA sample of $Sr_2[BN_2]Br$ after cooling from 1573 K showing the product is the mixture of $Sr_2[BN_2]Br$ and $Sr_3[BN_2]_2$.

Similarly, $Sr_2[BN_2]Br$ exhibits four exothermic and endothermic peaks at 903, 953K, 1243K and 1300K during heating. The former at 903K corresponds to the melting point of $SrBr_2$ while the exothermic peak 953K is indicating the reaction temperature. The endothermic peaks at 1243 and 1278K are assigned to the melting point of the product $Sr_2[BN_2]Br$ and its partial decomposition to $Sr_3[BN_2]_2$ and $SrBr_2$, respectively. During the cooling process, two sharp exothermic peaks were observed at 1244 which is interpreted as the crystallization temperatures for $Sr_2[BN_2]Br$, and at 1059K which we could not identify it yet but the further investigations are still in progress. X-ray powder diffraction measurement of the DTA sample (fig 3.3.7) shows that the product of DTA experiment is a

mixture of $Sr_2[BN_2]Br$, $Sr_3[BN_2]_2$ and $SrBr_2$. From DTA results, the ideal reaction temperature was determined as 1223 K, which is below the melting point of $Sr_2[BN_2]Br$.

3.3.3 Magnetic Susceptibility

The magnetic susceptibility measurements of $Eu_2[BN_2]Br$ were performed with a MPMS SQUID magnetic meter (Quantum Desing, Inc.) between 4.2 and 300 K with magnetic flux densities of up to 7 T. Before measurements, crystalline samples were sealed inside a quartz glass tube under 400 mbar pressure of helium gas.

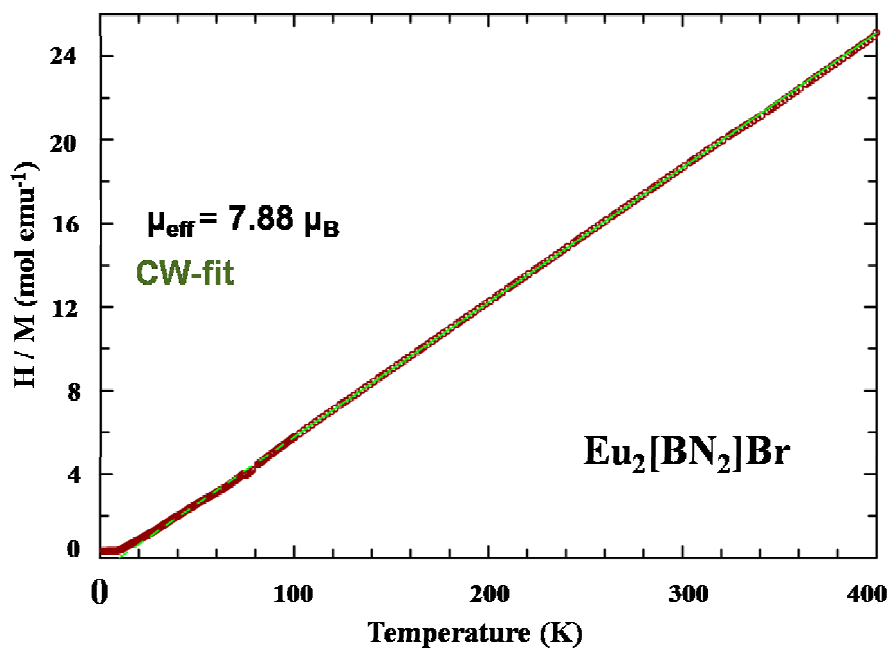


Fig 3.3.8 Temperature dependence of the reciprocal magnetic susceptibilities of $Eu_2[BN_2]Br$ determined at a magnetic flux density of 1T. .

The temperature dependency of the inverse magnetic susceptibilities (χ^{-1}) of $Eu_2[BN_2]Br$ is depicted in Figure 3.3.8. The susceptibilities of $Eu_2[BN_2]Br$ shows a Curie-Weiss paramagnetic behavior above 70K. The resulting effective magnetic moment of $\mu_{\text{exp}} = 7.88$

μ_{β} / Eu ($Eu_2[BN_2]Br$) obtained from the linear part of the $1/\chi$ vs T plot according to $\mu_{\text{exp}} = 2.83 [\chi/n(T-\Theta)]^{1/2} \mu_{\beta}$ [41]. compares well with the theoretical effective moment $\mu_{\text{eff}} = 7.94 \mu_B$ for a free Eu^{2+} ion calculated from $\mu_{\text{eff}} = g[J(J+1)]^{1/2} \mu_{\beta}$. The paramagnetic Curie Temperature (Weiss constant) $\Theta = 10.0$ (1) K was determined by extrapolation of the linear high temperature part of $1/\chi$ vs T plot to $1/\chi = 0$. The positive Weiss temperature Θ of 10.0 (1) K indicates ferromagnetic interactions

Chapter 4

$\text{Eu}_2[\text{BN}_2]\text{I}$

4.1 Synthesis

The compound $\text{Eu}_2[\text{BN}_2]\text{I}$ was obtained from a mixture of the binary components EuN , h-BN and EuI_2 . During the preparations of $\text{Eu}_2[\text{BN}_2]\text{I}$, 3: 2 :1,1 molar ($\Sigma m = 400 \text{ mg}$) mixtures of EuN , h-BN and EuI_2 were finely ground and mixed homogeneously. The mixtures were transferred into a clean niobium ampoule, arc-welded and sealed in an evacuated silica tube. The synthesis route followed for the reaction is based on single annealing of the reactant at 1273K for 24 hours then the reaction was cooled down to room temperature in 8 hours. The applied method yielded almost mono-phase products.

The reaction products were red to pale yellow plate-like air and moisture sensitive crystals. The purity of the reactions was investigated by using X-ray powder diffraction method. The analysis was performed by using Huber G670 with $\text{CuK}_{\alpha 1}$ radiation within $5^\circ \leq 2\theta \leq 85^\circ$ range. Fig 4.1.1 shows the comparison of observed powder diffractograms of $\text{Eu}_2[\text{BN}_2]\text{I}$ with the calculated powder patterns from single crystal analysis. The good agreements of the both theoretical and experimental patterns indicate the high purity of the samples.

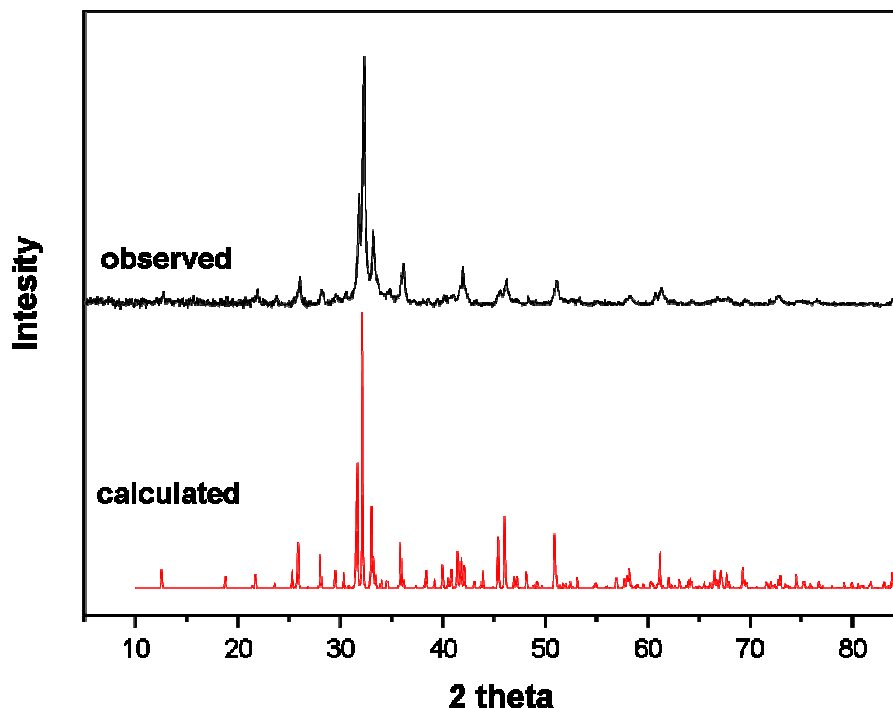


Fig 4.1.1 Observed and calculated X-ray Powder diffraction patterns of $\text{Eu}_2[\text{BN}_2]\text{I}$

4.2 Crystal Structure

The crystal structure of $\text{Eu}_2[\text{BN}_2]\text{I}$ was determined by single-crystal X-ray diffraction methods. The single crystal data were collected at room temperature on a Rigaku AFC7 four circle diffractometer equipped with a Mercury-CCD detector (MoK α radiation, graphite monochromator). After data collection the structures was solved by direct methods, using SHELXS-97 [30] and refined by using the full-matrix least-squares procedure SHELXL-97 [31].

$\text{Eu}_2[\text{BN}_2]\text{I}$ crystallizes in monoclinic space group ($P2_1 / m$ (No:11) with $a = 10.2548(6)$ Å, $b = 4.1587(3)$ Å, $c = 13.1234(9)$ Å, $\beta = 91.213(4)$, $Z = 4$, $V = 559.34$ Å³) and isotypic with $\text{Sr}_2[\text{BN}_2]\text{I}$ $\text{Sr}_2[\text{BN}_2]\text{I}$ and $\text{Eu}_2[\text{BN}_2]\text{I}$ have comparable lattice parameter due to the similarity of cationic radii between Sr^{2+} and Eu^{2+} [20]. The crystal structure can be

described by slightly puckered layers of edge sharing Br@Eu_6 distorted octahedra which are separated by isolated BN_2^{3-} anions. The BN_2^{3-} anions are arranged either parallel or perpendicular to the $[\text{Eu}_2\text{I}]^{3+}$ layers.(Fig. 4.2.1.) The bond lengths for the two crystallographically different $[\text{BN}_2]^{3-}$ anions are: $d(\text{B1-N3}) = 1.301(39) \text{ \AA}$, $d(\text{B1-N4}) = 1.352(36) \text{ \AA}$, $d(\text{B2-N1}) = 1.302(49) \text{ \AA}$ and $d(\text{B2-N2}) = 1.348(48) \text{ \AA}$, respectively. The bond angles vary slightly but significantly from the linearity: $\angle(\text{N3-B1-N4}) = 178.92(3)^\circ$ and $\angle(\text{N1-B2-N2}) = 172.90(4)^\circ$.

The crystal data and the conditions for data collection and refinement for $\text{Eu}_2[\text{BN}_2]\text{I}$ is summarized in Table 4.1.1 and Table 4.1.2 contain the atomic coordinates and displacement parameters and Table 4.1.3 depicts the important bond lengths and bond angles.

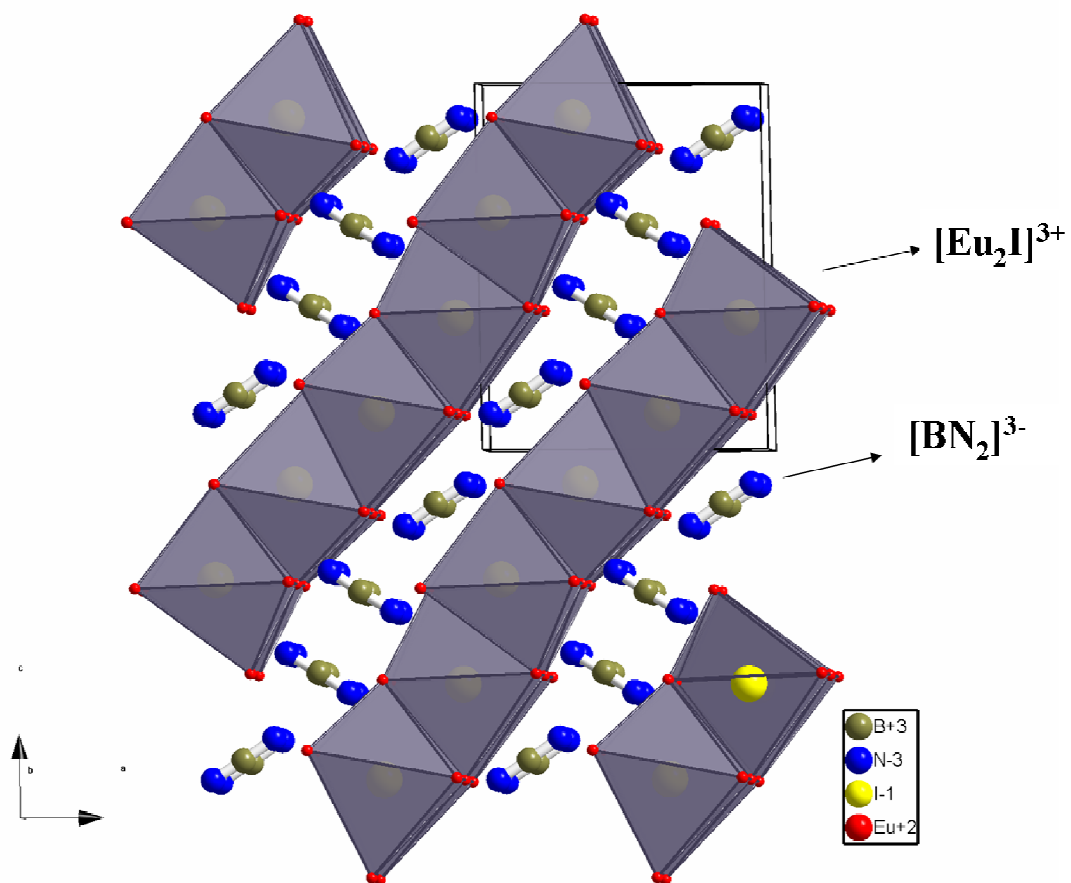


Fig 4.2.1 The crystal structure of $\text{Eu}_2[\text{BN}_2]\text{I}$

Compound	Eu ₂ [BN ₂]I
Crystal system	Monoclinic
Crystal color, shape, size	pale yellow plate
Space group	<i>P 1 21/m 1</i> (No. 11)
<i>Z</i>	4
<i>a</i> [Å]	10.2548(6)
<i>b</i> [Å]	4.1587(3)
<i>c</i> [Å]	13.1234(9)
β [°]	91.215(4)
<i>V</i> [Å ³]	559.34
<i>d</i> _x [g·cm ⁻³]	5.575
Diffractometer	Rigaku AFC 7
Detector	Mercury CCD
Monochromator	Graphite
Radiation, Wavelength	Mo K α , 0.71073
Scan mode	ϕ/ω
2 θ range [°]	62.72
No. Refl. Unique	1175
<i>R</i> _{int}	0.0476
Structure solution method	Direct Methods
Program for structure solution	SHELXS-97[30]
Program for structure refin.	SHELXL-97[31]
Refined parameters	9
Goof	1.176
<i>R</i> ₁ , <i>wR</i> ₂ (all data)	0.0784, 0.2558

Table 4.1 Refined crystallographic data for Eu₂[BN₂]I

Atom	Site	<i>X</i>	<i>Y</i>	<i>Z</i>	<i>U</i> _{iso} / <i>U</i> _{eq}
I1	2e	0.0769(2)	¼	0.6416(2)	0.0281(5)
I2	2e	0.6529(2)	¼	0.0952(2)	0.0280(5)
Eu1	2e	0.0790(1)	¼	0.9025(1)	0.0257(4)
Eu2	2e	0.6542(1)	¼	0.3667(1)	0.0248(4)
Eu3	2e	0.1925(1)	¼	0.3851(1)	0.0258(4)
Eu4	2e	0.6013(1)	¼	0.8277(1)	0.0259(4)
B1	2e	0.16094	¼	1.14816	

B2	2e	0.41744	¼	1.39084	
N1	2e	0.478(3)	¼	0.664(2)	0.0258(6)
N2	2e	0.693(3)	¼	0.557(2)	0.0229(5)
N3	2e	1.053(3)	¼	0.952(2)	0.0400(8)
N4	2e	0.271(3)	¼	0.208(2)	0.0190(5)

Table 4.2 Atomic coordinates and displacement parameters [in Å²] for Eu₂[BN₂]I. Standard deviations are given in parentheses.

<i>Atom</i>	<i>U</i> ₁₁	<i>U</i> ₂₂	<i>U</i> ₃₃	<i>U</i> ₁₂	<i>U</i> ₁₃	<i>U</i> ₂₃
Eu1	0.0258(8)	0.0308(9)	0.0203(9)	0	0	0
Eu2	0.0244(8)	0.0287(9)	0.0212(9)	0	-0.0035(6)	0
Eu3	0.0239(8)	0.0309(9)	0.0224(9)	0	-0.0015(6)	0
Eu4	0.0266(8)	0.0304(9)	0.0207(8)	0	-0.0035(6)	0
I1	0.0227(9)	0.033(1)	0.028(1)	0	0	0
I2	0.0243(9)	0.034(1)	0.025(1)	0	0	0

Table 4.3 Anisotropic displacement parameters [10⁻⁴ pm²] for Eu₂[BN₂]I, standard deviations of the last digit in parentheses

	<i>Atom 1</i>	<i>Atom 2</i>	<i>d</i> _{1,2} [Å]	<i>n</i>		<i>Atom 1</i>	<i>Atom 2</i>	<i>d</i> _{1,2} [Å]	<i>n</i>
I1–	Eu1	3.424(3)	1×	I2–	Eu1	3.446(2)	2×		
	Eu2	3.457(2)	2×		Eu2	3.562(3)	1×		
	Eu3	3.469(2)	2×		Eu4	3.500(2)	3×		
	Eu3	3.591(3)	1×						
B1–	N3	1.30(4)	1×	B2–	N1	1.30(5)			
	N4	1.35(4)	1×		N2	1.35(5)			
	Eu1	3.28(2)	2×		Eu2	3.19(3)	1×		
	Eu3	3.10(3)	1×		Eu2	3.25(4)	2×		
	Eu4	3.22(2)	2×		Eu3	3.13(3)	2×		
					Eu4	2.91(5)	1×		
		∠(N3–B1–N4)	178.92°			∠(N1–B2–N2)	172.9°		

Table 4.4 Selected atomic distances [Å] and bond angles [°] in Eu₂[BN₂]I with their multiplicity (*n*). Standard deviations are given in parentheses

4.3 Physical Properties

4.3.1 Infra-Red and Raman Spectroscopy

The spectroscopically relevant units in Eu₂[BN₂]I are the isolated [BN₂]³⁻ units with the idealized symmetry D_{∞h}. The distribution of the four fundamentals is as follows:

$$\Gamma_{\text{vib}} = \nu_1(\Sigma_g)(\text{R}) + \nu_2(\Sigma_u)(\text{IR}) + \nu_3(\Pi_u)(\text{IR}).$$

Because of the mutual exclusion, $\nu_1(\Sigma_g)$ is only Raman- while $\nu_2(\Sigma_u)$ and $\nu_3(\Pi_u)$ are exclusively IR-active.

In the crystal structure, the [BN₂]³⁻ moieties are occupying the sites *m*-Cs. Due to the symmetry reduction D_{∞h} → Cs the mutual exclusion is abolished for all three modes becoming now active both in IR and Raman. Furthermore, the double degenerate $\nu_3(\Pi_u)$ will split and two bands will be observed instead. The unit cell contains two crystallographically distinct (BN₂) units giving rise to additional splitting, so that $\nu_1(\Sigma_g)$ and $\nu_2(\Sigma_u)$ will appear as doublet each and $\nu_3(\Pi_u)$ as quartet in both spectra.

The vibrational spectra of Eu₂[BN₂]I are illustrated in Fig. 4.3.1. In accordance with the predictions the spectra are quite patterned revealing also the expected ¹⁰B / ¹¹B isotope. The symmetric (B-N) stretch splits and is registered only in the Raman spectrum: $\nu_{1a} = 1026 \text{ cm}^{-1}$ and $\nu_{1b} = 1034 \text{ cm}^{-1}$, respectively. $\nu_2(^{11}\text{B}/^{10}\text{B})$ are also split and observed at $\nu_{2a}(^{11}\text{B}) = 1690$ and $\nu_{2b}(^{11}\text{B}) = 1714 \text{ cm}^{-1}$, as well as at $\nu_{2a}(^{10}\text{B}) = 1742$ and $\nu_{2b}(^{10}\text{B}) = 1745 \text{ cm}^{-1}$, respectively.

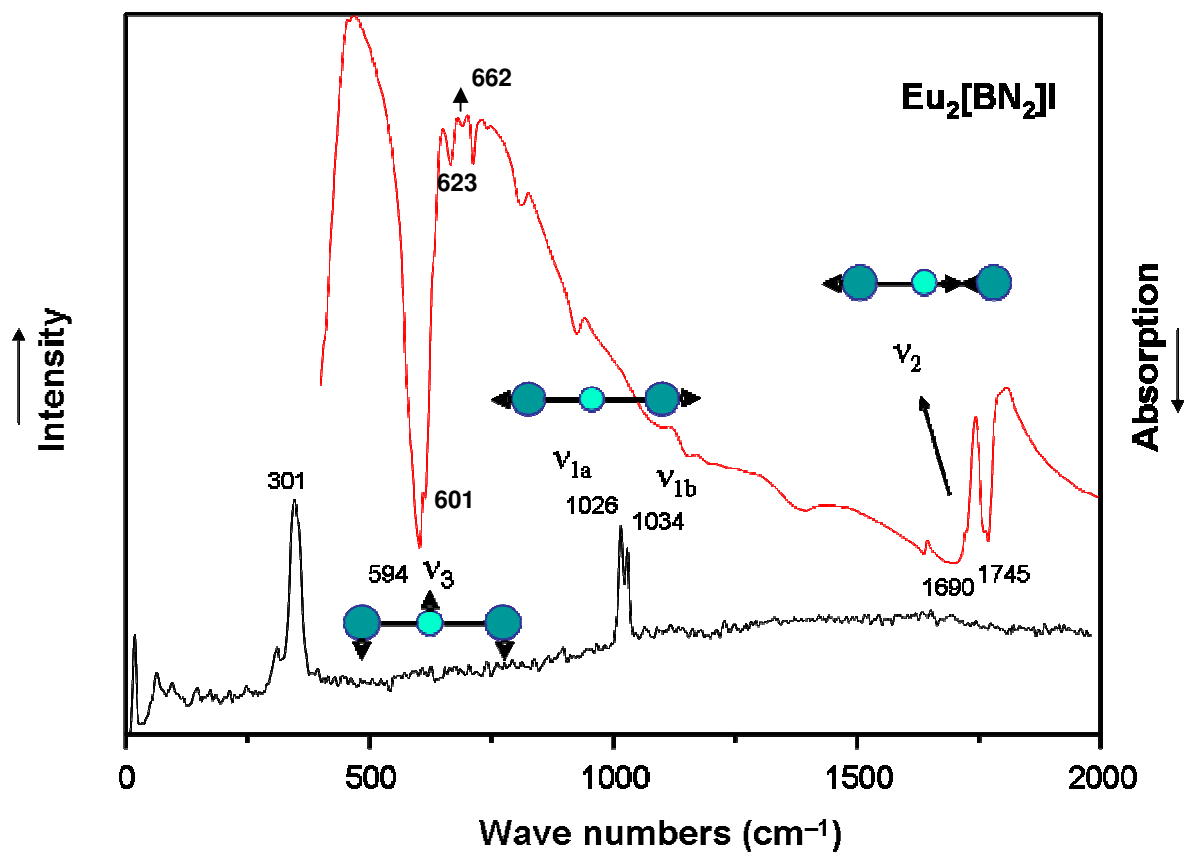


Fig 4.3.1 Vibrational Spectra of $\text{Eu}_2[\text{BN}_2]\text{I}$. A = Absorption and I = Intensity, both in arbitrary units.

The deformation mode reveals a multiplet consisting of two very strong, two weak bands, respectively. The former two are assigned as $\nu_{3a1} = 594$ (^{11}B) cm^{-1} and $\nu_{3a2} = 601$ (^{11}B) cm^{-1} while the remaining bands at 623 and 662 are resulting from the ($^{11}\text{B}/^{10}\text{B}$) splitting.

4.3.2 Magnetic Susceptibility

The magnetic susceptibility measurements of $\text{Eu}_2[\text{BN}_2]\text{I}$ were performed with a MPMS SQUID magnetic meter (Quantum Desing, Inc.) between 4.2 and 300 K with magnetic flux densities of up to 7 T. Before measurements, crystalline samples were sealed inside a quartz glass tube under 400 mbar pressure of helium gas.

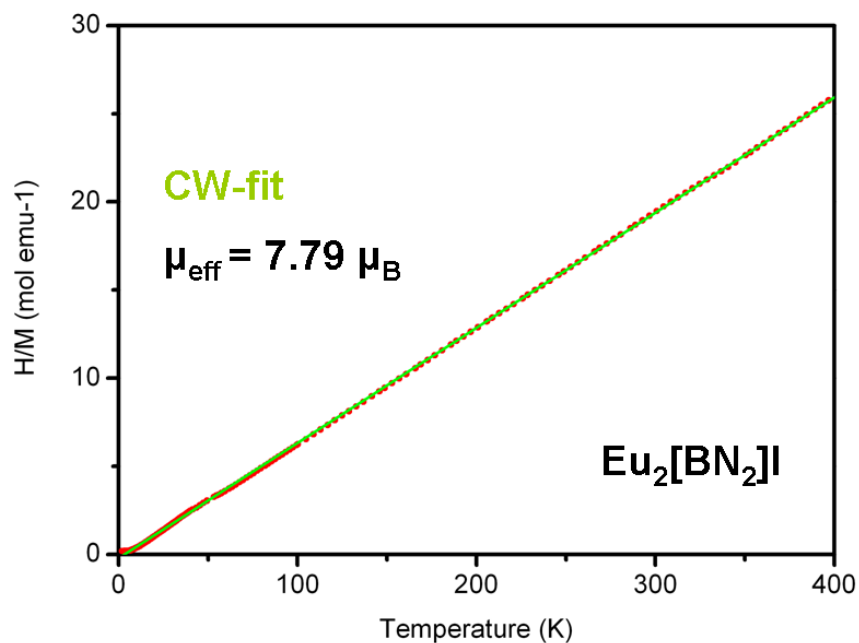


Fig 4.3.2 Temperature dependence of the reciprocal magnetic susceptibilities of $\text{Eu}_2[\text{BN}_2]\text{I}$ determined at a magnetic flux density of 1T.

The susceptibilities of $\text{Eu}_2[\text{BN}_2]\text{I}$ show Curie-Weiss paramagnetic behavior above 70 K (Figure 4.3.2) with a resulting magnetic moment of $\mu_{\text{exp}} = 7.79 \mu_{\text{B}} / \text{Eu}$ ($\text{Eu}_2[\text{BN}_2]\text{I}$) obtained from the linear part of the $1/\chi$ vs T plot and Curie Temperature (Weiss constant) $\Theta = +5.3$ (1) K obtained from the extrapolation of the linear high temperature part of the figure 4.3.4 which indicates ferromagnetic interactions.

Chapter 5

$\text{Eu}_3[\text{B}_3\text{N}_6]$ and $\text{Li}_{0.42}\text{Eu}_3[\text{B}_3\text{N}_6]$

5.1 Synthesis

$\text{Eu}_3[\text{B}_3\text{N}_6]$ was first observed as a minor phase in the synthesis of $\text{Eu}_2[\text{BN}_2]\text{Br}$ (CHP3 section 1). During the systematic investigation, it is also obtained as single phase from the oxidation reaction between $\text{Eu}_3[\text{BN}_2]_2$ and I_2 . $\text{Eu}_3[\text{B}_3\text{N}_6]$ is prepared as follows; 1 : 1 molar ($\Sigma m = 400$ mg) mixtures of $\text{Eu}_3[\text{B}_3\text{N}_6]$ and I_2 were put in an encapsulated Al_2O_3 crucible in evacuated silica tube.

$\text{Li}_{0.42}\text{Eu}_3[\text{B}_3\text{N}_6]$ was synthesized by using metathesis reaction between $\text{Li}_3[\text{BN}_2]$ and EuCl_3 . 1 : 1,1 molar ($\Sigma m = 400$ mg) mixtures of $\text{Li}_3[\text{BN}_2]$ and EuCl_3 were finely ground and mixed homogeneously. Then the mixture was transferred into a clean niobium ampoule which was arc-welded and sealed in an evacuated silica tube.

The reaction ampoules were placed in muffle furnace and heated up to 1073 K for $\text{Eu}_3[\text{B}_3\text{N}_6]$ and $\text{Li}_{0.42}\text{Eu}_3[\text{B}_3\text{N}_6]$. After 12 hours the reactions were cooled down to room temperature in 8 hours. The reaction product of $\text{Eu}_3[\text{B}_3\text{N}_6]$ is dark red crystals consisting of $\text{Eu}_3[\text{B}_3\text{N}_6]$ with trace amount of EuI_2 and The reaction product of $\text{Li}_{0.42}\text{Eu}_3[\text{B}_3\text{N}_6]$ is black column like crystals consisting of $\text{Li}_{0.42}\text{Eu}_3[\text{B}_3\text{N}_6]$ and LiCl . Since $\text{Eu}_3[\text{B}_3\text{N}_6]$ and $\text{Li}_{0.42}\text{Eu}_3[\text{B}_3\text{N}_6]$ are not moisture and air sensitive, they were extracted from the halides by just washing the mixture with water.

The purity of the reactions was investigated by using X-ray powder diffraction method. The analysis were performed by using Huber G670 with $\text{CuK}_{\alpha 1}$ radiation within $5^\circ \leq 2\theta \leq 85^\circ$ range. Fig 5.1.1 and Fig 5.1.2 shows the observed powder diffraction of $\text{Eu}_3[\text{B}_3\text{N}_6]$, $\text{Li}_{0.42}\text{Eu}_3[\text{B}_3\text{N}_6]$ and the calculated X-ray powder diffraction patterns from

single crystal measurements. The good agreements of the both theoretical and experimental patterns indicate the high purity of the samples.

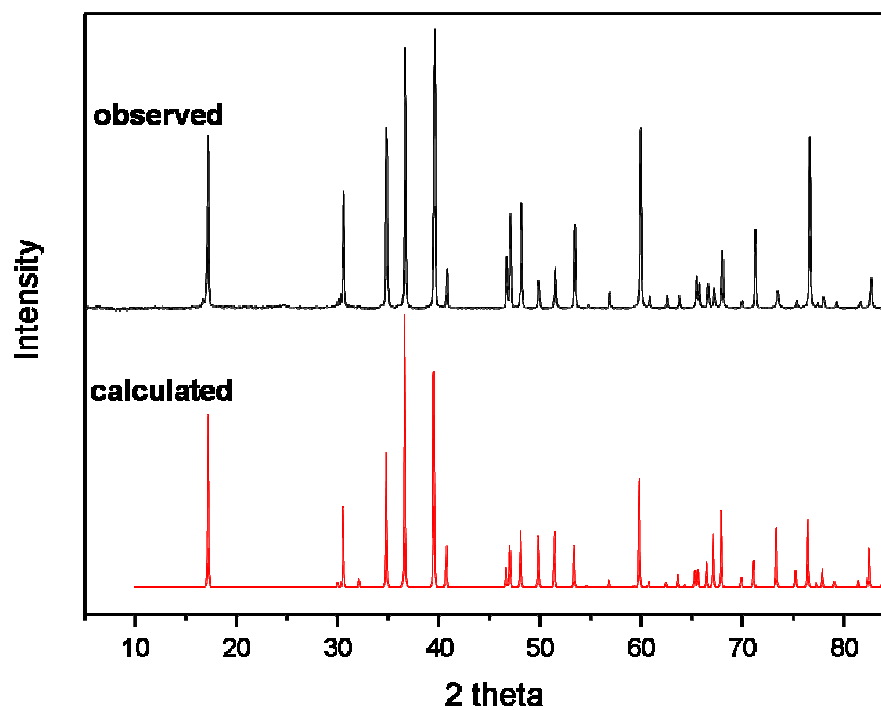


Fig 5.1.1 Observed and calculated X-ray Powder diffraction patterns of $\text{Eu}_3[\text{B}_3\text{N}_6]$

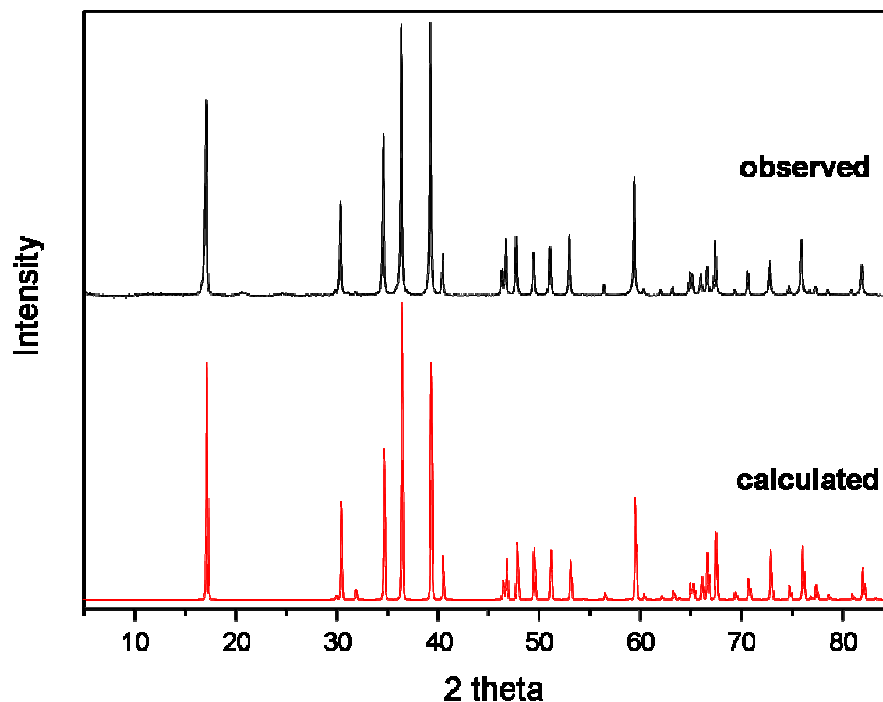


Fig 5.1.2 Observed and calculated X-ray Powder diffraction patterns of $\text{Li}_{0.42}\text{Eu}_3[\text{B}_3\text{N}_6]$

3.2 Crystal Structure

The crystal structures of $\text{Eu}_3[\text{B}_3\text{N}_6]$ and $\text{Li}_{0.42}\text{Eu}_3[\text{B}_3\text{N}_6]$ were determined by single-crystal X-ray diffraction methods. The single crystal data were collected at room temperature on a Rigaku AFC7 four circle diffractometer equipped with a Mercury-CCD detector (MoK_{α} radiation, graphite monochromator). After data collection the structures was solved by direct methods, using SHELXS-97 [30] and refined by using the full-matrix least-squares procedure SHELXL-97 [31].

$\text{Eu}_3[\text{B}_3\text{N}_6]$ (**1**) and $\text{Li}_{0.42}\text{Eu}_3[\text{B}_3\text{N}_6]$ (**2**) crystallize in the trigonal space group $R\bar{3}c$ (No:167) with $a = 11.9559(1)$ Å, $c = 6.8140(6)$ Å and $Z = 6$ for (**1**) and $a = 12.0225(2)$ Å, $c = 6.8556(2)$ Å and $Z = 6$ for (**2**). The crystal structure (Fig 5.2.1) of $\text{Eu}_3[\text{B}_3\text{N}_6]$ consists of isolated, planar cyclic $[\text{B}_3\text{N}_6]^{9-}$ units along $[001]$ charge-balanced by Eu^{3+} cations. Each

endo-cyclic nitrogen atom resides in a very distorted tetrahedra of 2Eu and 2 B atom (Fig 5.2.2). And each exo-cyclic nitrogen atom in $[\text{B}_3\text{N}_6]^{9-}$ units resides in a distorted square pyramid of Eu atoms (Fig 5.2.3). In addition to these, coordination around Eu is 7 (Fig. 5.2.4)

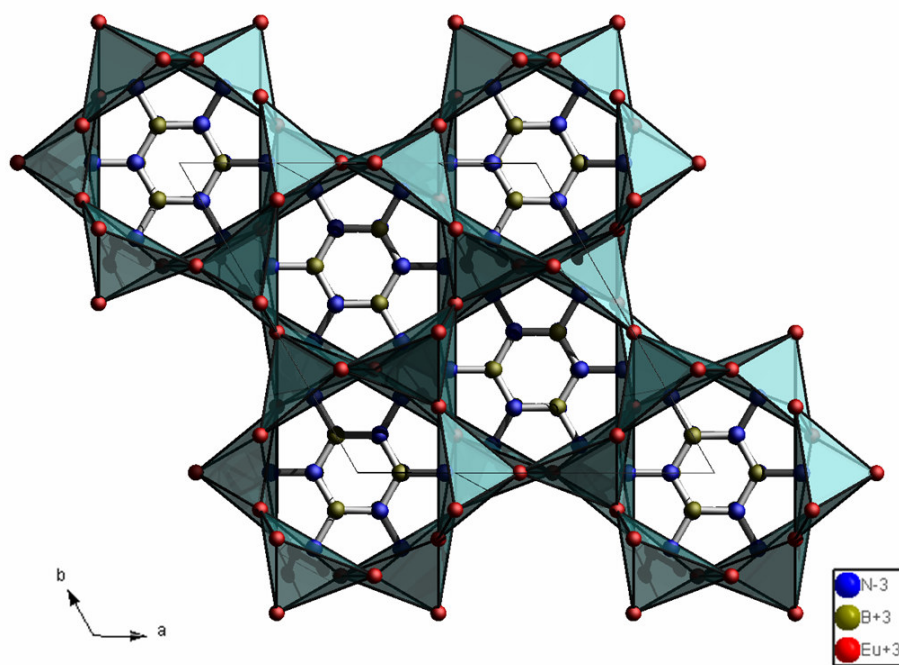


Fig 5.2.1 The crystal structure of $\text{Eu}_3[\text{B}_3\text{N}_6]$

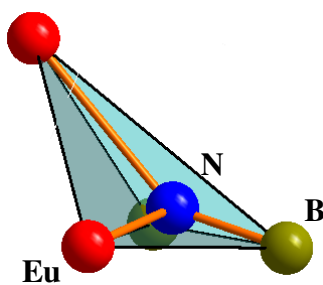


Fig 5.2.2 Tetrahedral coordination of Eu and B around endo-cyclic N

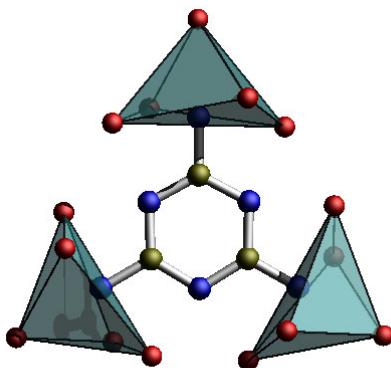


Fig 5.2.3 Cyclic $[\text{B}_3\text{N}_6]^{9-}$ units and polyhedra

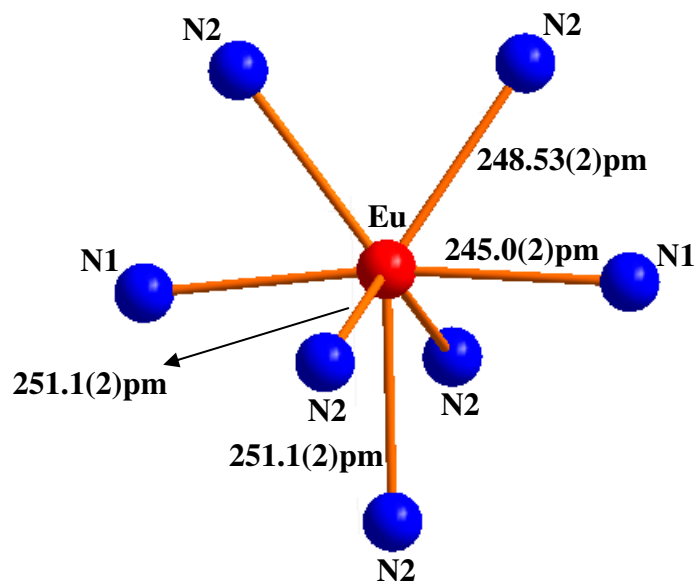


Fig 5.2.4 Local coordination for Eu

The crystal structure of $\text{Li}_{0.42}\text{Eu}_3[\text{B}_3\text{N}_6]$. (Fig 5.2.5) again consists of isolated, planar cyclic $[\text{B}_3\text{N}_6]^{9-}$ units along $[001]$ but they are charge-balanced by the mixed valence $\text{Eu}^{3+}/\text{Eu}^{2+}$ and Li^+ cations. Li^+ occupies statistically (42%) the sites $36f$ and is sandwiched between

the $[\text{B}_3\text{N}_6]^{9-}$ anions (Fig 5.2.6) and each exo-cyclic nitrogen atom in $[\text{B}_3\text{N}_6]^{9-}$ units resides in a distorted square pyramid of $\text{Eu}^{3+}/\text{Eu}^{2+}$ cations.

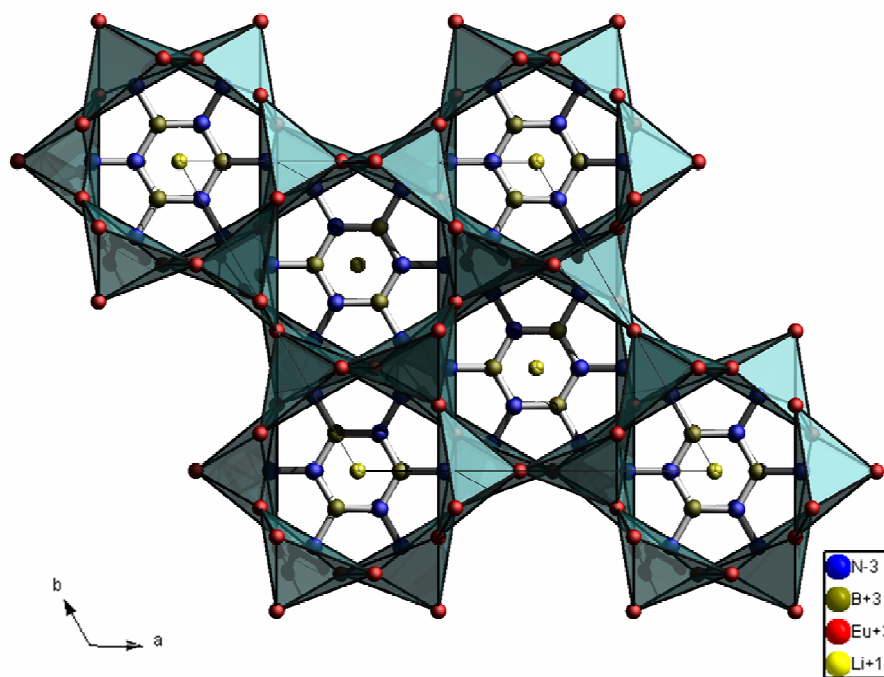


Fig 5.2.5 The crystal structure of $\text{Li}_{0.42}\text{Eu}_3[\text{B}_3\text{N}_6]$

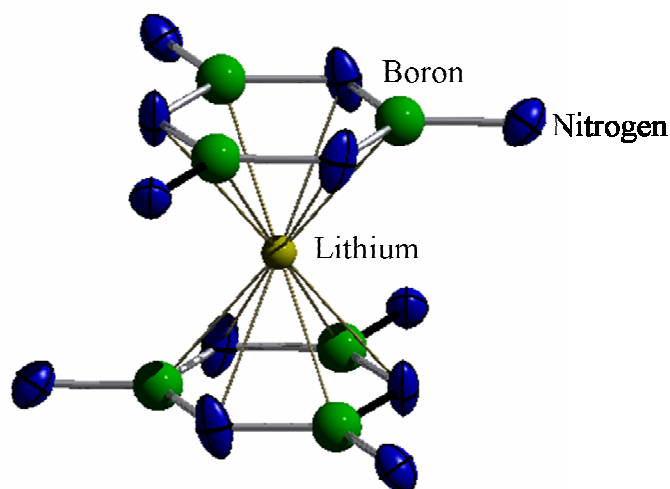


Fig 5.2.6 Cyclic $[\text{B}_3\text{N}_6]^{9-}$ units in structure

The endo and exocyclic bond lengths within the $[\text{B}_3\text{N}_6]^{9-}$ groups are practically $d(\text{B-N})_{\text{exo}} = 1.466(2) \text{ \AA}$, $d(\text{B-N})_{\text{endo}} = 1.475(4) \text{ \AA}$ for both $\text{Eu}_3[\text{B}_3\text{N}_6]$ and $\text{Li}_{0.42}\text{Eu}_3[\text{B}_3\text{N}_6]$ and bond angles are $\angle(\text{N-B-N}) = 123.1(3)^\circ$ ($2\times$) and $\angle(\text{N}_{\text{endo}}\text{-B-N}_{\text{exo}}) = 118.4(1)^\circ$ for $\text{Eu}_3[\text{B}_3\text{N}_6]$ and $\angle(\text{N-B-N}) = 122.9(5)^\circ$ ($2\times$) and $\angle(\text{N}_{\text{endo}}\text{-B-N}_{\text{exo}}) = 118.5(3)^\circ$ for $\text{Li}_{0.42}\text{Eu}_3[\text{B}_3\text{N}_6]$. The Boron endocyclic nitrogen distances in the $[\text{B}_3\text{N}_6]^{9-}$ unit are slightly longer (1.474 \AA) than exocyclic nitrogen atoms (1.464 \AA). Six-member $[\text{B}_3\text{N}_6]^{9-}$ units can also be considered as one fragment of the hexagonal BN layer. When we compare the observed B-N distances between title compounds with h-BN (145 pm) and $\text{B}_3\text{N}_3\text{H}_6$ (143 pm) [42], $[\text{B}_3\text{N}_6]^{9-}$ units have slightly larger B-N distances because of anionic character of the $[\text{B}_3\text{N}_6]^{9-}$ units.

Compound	$\text{Eu}_3[\text{B}_3\text{N}_6]$	$\text{Li}_{0.42}\text{Eu}_3[\text{B}_3\text{N}_6]$
Crystal system	Trigonal	Trigonal
Crystal color, shape, size	Black, hexagonal-column	Black, hexagonal-column
Space group	$R\bar{3}c$ (No. 167)	$R\bar{3}c$ (No. 167)
Z	6	6
a [Å]	11.9559(1)	12.0255(2)
b [Å]	11.9559(1)	12.0255(2)
c [Å]	6.8140(6)	6.8556(2)
V [Å ³]	843.52	858.15
d_x [g·cm ⁻³]	6.55926	6.86276
Diffractometer	Rigaku AFC 7	Rigaku AFC 7
Detector	Mercury CCD	Mercury CCD
Monochromator	Graphite	Graphite
Radiation, Wavelength	Mo K_α , 0.71073	Mo K_α , 0.71073
Scan mode	ϕ/ϕ	ϕ/ϕ
2θ range [°]	138.40	57.95
No. Refl. unique	3573	257
R_{int}	0.1180	0.0188
Structure solution method	Direct Methods	Direct Methods
Program for structure solution	SHELXS-97[30]	SHELXS-97[30]
Program for structure refin.	SHELXL-97[31]	SHELXL-97[31]
Refined parameters	22	25
Goof	0.70	1.179
R_1, wR_2 (all data)	0.046, 0.1427	0.0127, 0.0257

Table 5.1 Crystallographic data and refinement details for $\text{Eu}_3[\text{B}_3\text{N}_6]$ and $\text{Li}_{0.42}\text{Eu}_3[\text{B}_3\text{N}_6]$

Atom	Site	x	y	z	U_{iso} / U_{eq}	Occ. (%)
Eu	18e	0.4540(1)	0	0	0.0069(1)	1
B	18e	0.1207(2)	0	¼	0.0069(3)	1
N1	18e	0.8754(2)	0	¼	0.0089(2)	1
N2	18e	0.2440(1)	0	¼	0.0075(2)	1

Table 5.2 Atomic coordinates and displacement parameters [in Å²] for $\text{Eu}_3[\text{B}_3\text{N}_6]$. Standard deviations are given in parentheses

Atom	Site	<i>x</i>	<i>y</i>	<i>z</i>	$U_{\text{iso}} / U_{\text{eq}}$	Occ. (%)
Li	6b	0	0	0	0.0070(11)	0.42
Eu	18e	0.4533(2)	0	0	0.0063(1)	1
B	18e	0.1197(5)	0	¼	0.0065(10)	1
N1	18e	0.8766(3)	0	¼	0.0106(8)	1
N2	18e	0.2434(3)	0	¼	0.0119(9)	1

Table 5.3 Atomic coordinates and displacement parameters [in Å²] for $\text{Li}_{0.42}\text{Eu}_3[\text{B}_3\text{N}_6]$. Standard deviations are given in parentheses.

Atom 1	Atom 2	d1,2[Å]	n	Atom 1	Atom 2	d1,2[Å]	n
Eu–	N1	2.450(2)	2×	B–	N2	1.475(4)	1×
	N2	2.4853(2)	2×		N1	1.466(2)	2×
	N2	2.511(2)	1×				
	N2	2.6156(4)	2×				
		∠(N1–B–N1)	123.1(3)°				
		∠(N1–B–N2)	118.4(1)°				

Table 5.4 Selected atomic distances [Å] and bond angles [°] in $\text{Eu}_3[\text{B}_3\text{N}_6]$ with their multiplicity (n). Standard deviations are given in parentheses

Atom 1	Atom 2	d1,2[Å]	n	Atom 1	Atom 2	d1,2[Å]	n
Eu–	N1	2.473(3)	2×	B–	N2	1.486(7)	1×
	N2	2.5062(4)	2×		N1	1.462(3)	2×
	N2	2.523(4)	1×				
	N2	2.6291(6)	2×				
		∠(N1–B–N1)	122.9(5)°				
		∠(N1–B–N2)	118.5(3)°				

Table 5.5 Selected atomic distances [Å] and bond angles [°] in $\text{Li}_{0.42}\text{Eu}_3[\text{B}_3\text{N}_6]$ with their multiplicity (n). Standard deviations are given in parentheses

Atom	U_{11}	U_{22}	U_{33}	U_{12}	U_{13}	U_{23}
Eu1	0.00641(3)	0.00743(4)	0.00709(4)	0.00372(2)	0.00102(1)	0.0025(2)
B1	0.0058(5)	0.0070(7)	0.0080(7)	0.0035(4)	0.0003(3)	0.0006(6)
N1	0.0061(3)	0.0064(5)	0.0143(7)	0.0032(2)	-0.0011(2)	-0.0143(7)
N2	0.0058(3)	0.0089(6)	0.0089(5)	0.0044(3)	-0.0004(2)	-0.0009(4)

Table 5.6 Anisotropic displacement parameters [10^{-4} pm^2] for $\text{Eu}_3[\text{B}_3\text{N}_6]$, standard deviations of the last digit in parentheses

Atom	U_{11}	U_{22}	U_{33}	U_{12}	U_{13}	U_{23}
Eu1	0.0057(1)	0.0067(1)	0.0069(1)	0.00335(7)	0.00105(4)	0.00210(8)
N1	0.010(1)	0.011(2)	0.012(2)	0.005(1)	-0.0018(8)	-0.004(1)
N2	0.006(1)	0.010(2)	0.021(2)	0.005(1)	-0.0006(8)	-0.001(1)

Table 5.7 Anisotropic displacement parameters [10^{-4} pm^2] for $\text{Li}_{0.42}\text{Eu}_3[\text{B}_3\text{N}_6]$, standard deviations of the last digit in parentheses

5.3 Physical Properties

5.3.2 Magnetic Susceptibility

The magnetic susceptibility measurements of $\text{Eu}_3[\text{B}_3\text{N}_6]$ and $\text{Li}_{0.42}\text{Eu}_3[\text{B}_3\text{N}_6]$ were performed with a MPMS SQUID magnetic meter (Quantum Design, Inc.) between 4.2 and 300 K with magnetic flux densities of up to 7 T. Before measurements, crystalline samples were sealed inside a quartz glass tube under 400 mbar pressure of helium gas

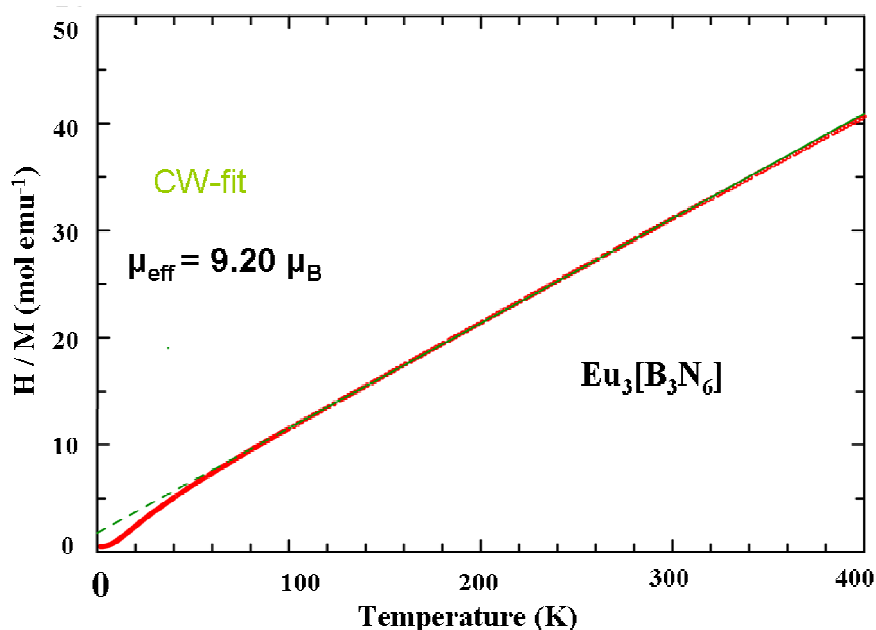


Fig 5.3.1 Temperature dependence of the reciprocal magnetic susceptibilities of $\text{Eu}_3[\text{B}_3\text{N}_6]$ determined at a magnetic flux density of 1T.

The temperature dependency of the inverse magnetic susceptibilities (χ^{-1}) of $\text{Eu}_3[\text{B}_3\text{N}_6]$ is shown in Figure 5.3.1. The susceptibilities of $\text{Eu}_3[\text{B}_3\text{N}_6]$ shows a Curie-Weiss paramagnetic behavior above 70K. The resulting effective magnetic moment of $\mu_{\text{exp}} = 9.20 \mu_{\text{B}} / \text{Eu}$ obtained from the linear part of the $1/\chi$ vs T plot according to $\mu_{\text{exp}} = 2.83 [\chi/n(T-\Theta)]^{1/2} \mu_{\text{B}}$ [45]. The paramagnetic Curie Temperature (Weiss constant) $\Theta = -18.1(1) \text{ K}$ was determined by extrapolation of the linear high temperature part of $1/\chi$ vs T plot to $1/\chi = 0$. The negative Weiss temperature Θ of $-18.1(1) \text{ K}$ indicates anti-ferromagnetic interactions.

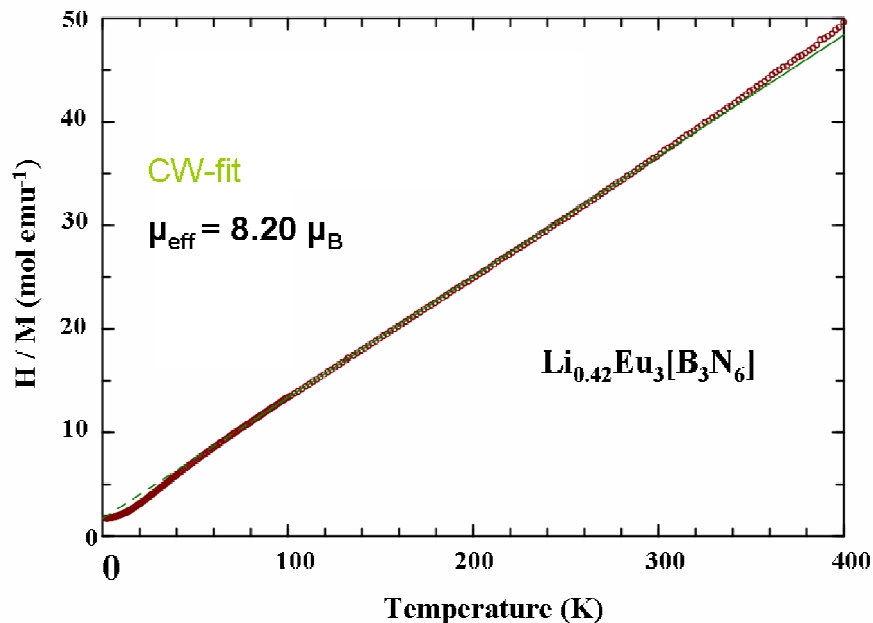


Fig 5.3.2 Temperature dependence of the reciprocal magnetic susceptibilities of $\text{Li}_{0.42}\text{Eu}_3[\text{B}_3\text{N}_6]$ determined at a magnetic flux density of 3.5T.

Inverse magnetic susceptibilities of $\text{Li}_{0.42}\text{Eu}_3[\text{B}_3\text{N}_6]$ as a function of temperature in the magnetic field of 3.5T is presented in Figure 5.3.2. The susceptibilities obey the Curie-Weiss law above 80K. The experimental magnetic moment of $\mu_{\text{eff}} = 8.28 \mu_{\text{B}}$ and $\Theta = -14.6 \text{ K}$ (non-linear) and $\mu_{\text{eff}} = 8.20 \mu_{\text{B}}$ and $\Theta = -11.0 \text{ K}$ (linear). These results show that 1 out of three atoms could be magnetic. But since only one europium site exist in the structure so that leads the conclusion as 36 % of the Europium are Eu^{2+} and no trace of EuO was observed ($0.1 < \text{mass } \%$)

5.3.3 Electron Spin Resonance Spectroscopy

The powder samples of $\text{Eu}_3[\text{B}_3\text{N}_6]$ and $\text{Li}_{0.42}\text{Eu}_3[\text{B}_3\text{N}_6]$ were investigated via X-Band ESR (9,4 GHz) in a temperature range between 5 and 300K. The ESR spectra of the title compounds are shown in Fig. 5.3.3 and Fig 5.3.4

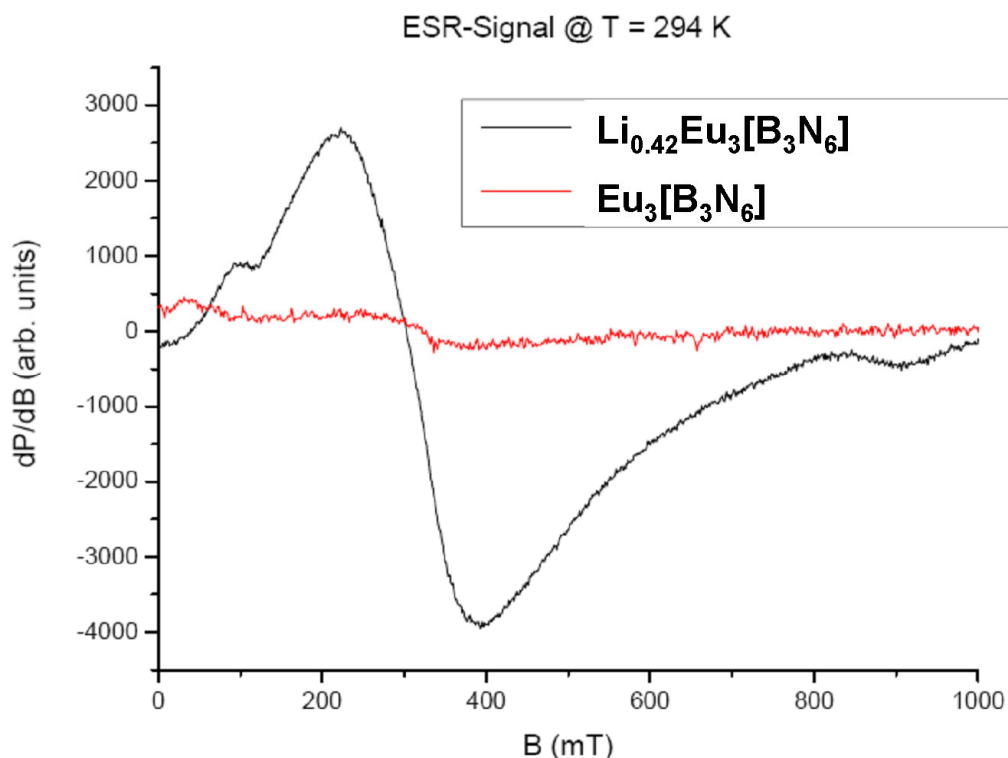


Fig 5.3.3 Electron Spin Resonance spectra of $\text{Li}_{0.42}\text{Eu}_3[\text{B}_3\text{N}_6]$ (black) and $\text{Eu}_3[\text{B}_3\text{N}_6]$ (red) at 294K.

Eu^{2+} ion with the $4f^7$ configuration and $^8\text{S}_{7/2}$ ground level can be easily detected, whereas the detection of the Eu^{3+} ion with a non-magnetic ($J=0$) $^7\text{F}_0$ ground level of the $4f^6$ configuration is almost impossible by EPR. In this respect, the existence of Eu^{2+} in $\text{Li}_{0.42}\text{Eu}_3[\text{B}_3\text{N}_6]$ can clearly be seen in the ESR spectra of the $\text{Li}_{0.42}\text{Eu}_3[\text{B}_3\text{N}_6]$ (black) (Fig 5.3.3) at 294K, which is composed of very broad features between 210 and 400 mT and definitely there are some paramagnetic species in $\text{Li}_{0.42}\text{Eu}_3[\text{B}_3\text{N}_6]$ because of the strong signal centered around 320mT. According to the $4f^6$ configuration of the Eu^{3+} in the $\text{Eu}_3[\text{B}_3\text{N}_6]$ (red), it is ESR inactive.

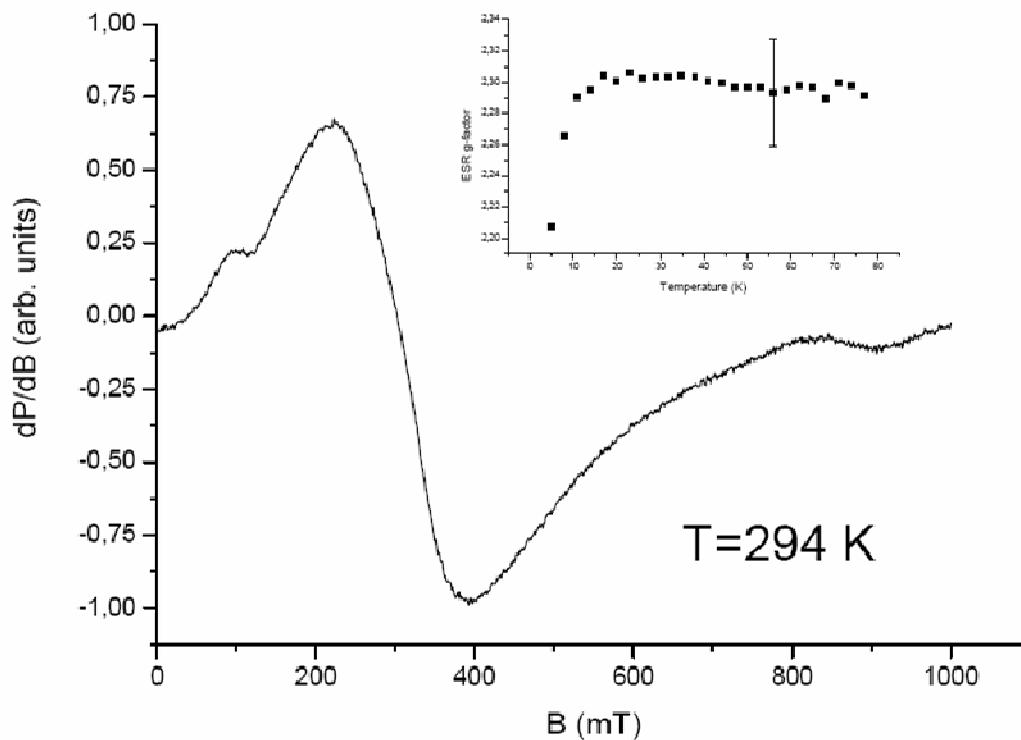


Fig 5.3.4 The X-Band ESR Spectra of $\text{Li}_{0.42}\text{Eu}_3[\text{B}_3\text{N}_6]$ at 294K is presented together with temperature dependency of g factor.

$\text{Li}_{0.42}\text{Eu}_3[\text{B}_3\text{N}_6]$ shows an intense signal over the whole temperature range. Superposition of broad and narrow lines is observed at room temperature X-Band ESR spectrum (**Fig 5.3.4**), g-factors of both lines are originating from Eu^{2+} and temperature independent down to 11 K (*inset Fig 5.3.4 only for broad line*)

5.3.4 Mössbauer Spectroscopy

The 21.53 keV transition of ^{151}Eu with an activity of 130 MBq (2% of the total activity of a $^{151}\text{Sm}:\text{EuF}_3$ source) was used for the Mössbauer spectroscopic experiment which was conducted in the usual transmission geometry. The measurement was performed with a commercial helium bath cryostat. The temperature of the absorber was kept at 78 K, while the source was kept at room temperature. The sample was placed within a thin-walled glass container sealed with an ultra-violet glue. The thickness of the sample corresponded to about 10 mg Eu/cm^2 .

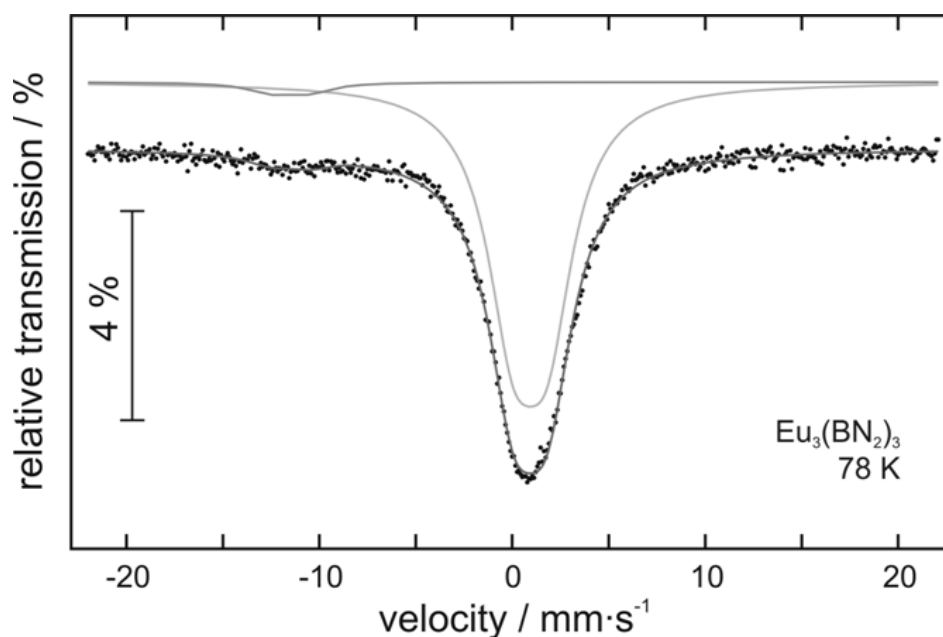


Fig 5.3.5 The ^{151}Eu Mössbauer spectra of $\text{Eu}_3[\text{B}_3\text{N}_6]$ at 78 K is presented together with a transmission integral fits

The ^{151}Eu Mössbauer spectrum of $\text{Eu}_3(\text{BN}_2)_3$ at 78 K is presented in Figure 5.3.5 together with a transmission integral fit. The spectrum shows one main signal at an isomer shift $\delta = 0.93(7)$ mm/s and a line width of $\Gamma = 3.31(3)$ mm/s. Due to the non-cubic site

symmetry, the signal is subjected to quadrupole splitting of $\Delta E_Q = 1.75(2)$ mm/s. The low isomer shift is unambiguously indicating trivalent europium in $\text{Eu}_3(\text{BN}_2)_3$. A very weak additional signal (ca. 3 % of the sample) is detected at $\delta = -11.6(2)$ mm/s with $\Delta E_Q = 2.0(3)$ mm/s, most likely due a trace amount of a Eu^{2+} containing impurity. This isomer shift is close the value of $\text{Eu}_3(\text{BN}_2)_2$ (-11.4 mm/s) [43].

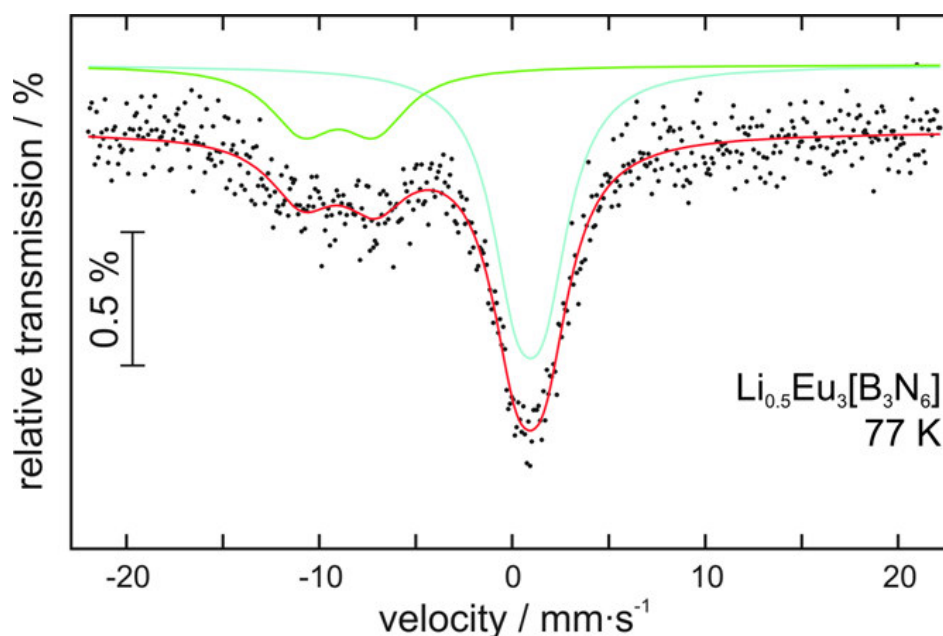


Fig 5.3.6 The ^{151}Eu Mössbauer spectra of $\text{Li}_{0.42}\text{Eu}_3[\text{B}_3\text{N}_6]$ at 77 K is presented together with a transmission integral fits.

The ^{151}Eu Mössbauer spectra of $\text{Li}_{0.42}\text{Eu}_3[\text{B}_3\text{N}_6]$ was recorded at 77 K and illustrated together with a transmission integral fits in Figure 5.3.6. The fitting parameters are $\delta = 0.99(4)$ mm/s, $\Gamma = 3.7(2)$ mm/s and $\Delta E_Q = 1.7(2)$ mm/s for the Eu^{3+} signal and $\delta = -10.3(3)$ mm/s, $\Gamma = 4.6(5)$ mm/s and $\Delta E_Q = 4.3(3)$ mm/s for the Eu^{2+} signal in an area ratio of 2.3(2) : 1. The values of the isomer shifts compare well with the data of $\text{Eu}_3(\text{BN}_2)_2$ (-11.4 mm/s) [43] with purely divalent europium and $\text{Eu}_3[\text{B}_3\text{N}_6]$ ($0.93(7)$ mm/s) with purely trivalent europium.

Chapter 6

COUNCLUSIONS

In the present study, quaternary nitridoborate system M/B/N/X (M = Ca, Sr, Eu and X = Br, I) has been investigated in terms of their syntheses, crystal structures, as well as thermal and magnetic properties. The synthesis attempts of quaternary nitridoborate $\text{Eu}_2[\text{BN}_2]\text{Br}$ from EuBr_2 , BN and EuN, yielded $\text{Eu}_3[\text{B}_3\text{N}_6]$, the first nitridoborate in which Eu exists solely the oxidation state +3. A different synthesis route for $\text{Eu}_3[\text{B}_3\text{N}_6]$ via metathesis reaction of EuCl_3 with and LiCl led surprisingly to another novel nitridoborate, $\text{Li}_{0.42}\text{Eu}_3[\text{B}_3\text{N}_6]$, in which Eu is in mixed valence state ($\text{Eu}^{2+}/\text{Eu}^{3+}$).

The compound series $\text{M}_2[\text{BN}_2]\text{Br}$ (M = Ca, Sr, Eu) crystallize in the space group $R\bar{3}m$ (Pearson code $hR6$; Z = 3) with $a = 3.86897(7)\text{\AA}$, $c = 25.8135(6)\text{\AA}$ for $\text{Ca}_2[\text{BN}_2]\text{Br}$, $a = 4.117\text{\AA}$, $c = 26.487$ for $\text{Sr}_2[\text{BN}_2]\text{Br}$ and $a = 4.0728\text{\AA}$, $c = 26.5890\text{\AA}$ for $\text{Eu}_2[\text{BN}_2]\text{Br}$. They are isotypic to $\text{Sr}_2[\text{CuO}_2]\text{Br}$. As for the monoclinic $\text{Eu}_2[\text{BN}_2]\text{I}$ (space group: $P2_1/m$, No:11, $a = 10.2548\text{\AA}$, $b = 4.1587\text{\AA}$, $c = 13.1234\text{\AA}$, $\beta = 91.21$, Z = 4) - which is isotypic with $\text{Sr}_2[\text{BN}_2]\text{I}$ - the crystal structures are built up by isolated rod like $[\text{N-B-N}]^{3-}$ units and spherical X^- moieties. Unlike for the hitherto known dinitridoborate halides, the two differently shaped anions in $\text{M}^{\text{II}}_2[\text{BN}_2]\text{Br}$ ($\text{M}^{\text{II}} = \text{Ca}, \text{Sr}, \text{Eu}$) are coordinated for the first time by same type of polyhedra (trigonal antiprisms) formed by the counterions M^{II} . As a result, the anions are spatial no more strictly separated, but and slightly disordered (mixed occupancy).

The isolated linear $[\text{BN}_2]^{3-}$ units in $\text{M}^{\text{II}}_2[\text{BN}_2]\text{Br}$ ($\text{M}^{\text{II}} = \text{Ca}, \text{Sr}, \text{Eu}$; X = Br, I) and $\text{Eu}_2[\text{BN}_2]\text{I}$ were investigated by vibrational spectroscopy and in case of the europium

compounds also by magnetic measurements. The vibrational spectra were interpreted based on the idealized symmetry $D_{\infty h}$ of the spectroscopic relevant $[\text{BN}_2]^{3-}$ groups. The susceptibilities for $\text{Eu}_2[\text{BN}_2]\text{X}$ ($\text{X} = \text{Br}, \text{I}$) shows a Curie-Weiss paramagnetic behavior and the resulting effective magnetic moments compare well with the theoretical effective moment for a free Eu^{2+} ion [48].

$\text{Eu}_3[\text{B}_3\text{N}_6]$ (**1**) and $\text{Li}_{0.42}\text{Eu}_3[\text{B}_3\text{N}_6]$ (**2**) crystallizes in the trigonal space group $R\bar{3}c$ (No:167) with $a = 11.9559(2)$ Å, $c = 6.814(2)$ Å and $Z = 6$ (**1**) and $a = 12.0225(2)$ Å, $c = 6.8556(2)$ Å and $Z = 6$ (**2**). Partial anionic structures are built up by isolated, planar cyclic $[\text{B}_3\text{N}_6]^{9-}$ units which are surrounded by bi capped polyhedra of Eu^{+3} atoms for (**1**) and mixed valence $\text{Eu}^{3+}/\text{Eu}^{2+}$ atoms for (**2**). In $\text{Li}_{0.42}\text{Eu}_3[\text{B}_3\text{N}_6]$, Li^+ occupies statistically (42%) the sites $36f$ to charge balance and it is sandwiched between the $[\text{B}_3\text{N}_6]^{9-}$ anions. Both compounds reveal an interesting electronic behavior in terms of the valance state and magnetic interaction. for the determination of the valance states in (**1**) and (**2**), Electron spin resonance (ESR) and Mössbauer spectroscopy, as well as magnetic measurements were employed for the determination of the valance states.. According to the ESR spectroscopic results, $\text{Eu}_3[\text{B}_3\text{N}_6]$ is - as expected for Eu^{3+} - ESR inactive - while $\text{Li}_{0.42}\text{Eu}_3[\text{B}_3\text{N}_6]$ is ESR active. The latter exhibits a broad signal between 210 and 400 mT which is consistent with the presence divalent Eu ions. The results of the Mössbauer spectroscopy are also confirming the mixed valancy of Eu atom in $\text{Li}_{0.42}\text{Eu}_3[\text{B}_3\text{N}_6]$ by showing both the doublet (quadruple splitting) and single resonance lines of Eu^{2+} and Eu^{3+} , respectively. Above 80K, $\text{Li}_{0.42}\text{Eu}_3[\text{B}_3\text{N}_6]$ shows Curie-Weiss behavior with an experimental effective magnetic moment of $\mu_{\text{eff}} = 8.28$, slightly higher than the theoretical effective magnetic moment of $\mu_{\text{eff}} = 7.94$.

Concerning the material's properties, the most promising compound in this study is $\text{Li}_{0.42}\text{Eu}_3[\text{B}_3\text{N}_6]$ which is expected to be a lithium ion conductor. All attempts to record a reproducible impedance spectrum failed yet, due to the lack suitable large single crystals.

The related activities of measuring the Li-ion conductivity on hot-pressed pellets of $\text{Li}_{0.42}\text{Eu}_3[\text{B}_3\text{N}_6]$ are proceeding in close cooperation with the Renewable Energy Department at Technical University of Eindhoven.

BIBLIOGRAPHY

- [1] J. Goubeau and W. Anselment, *Z. Anorg. Allg. Chem.* **1961**, 310, 248.
- [2] T. Sato, T. Endo, S. Kashima, O. Fukunaga, and M. Iwata, *J. Mater. Sci.* **1983**, 18, 3054.
- [3] Y. Yamane, S. Kikkawa, M. Koizumi, *J. Solid State Chem.* 1987, 71, 1.
- [4] J. Evers, M. Münsterkötter, G. Oehlinger, K. Polborn, B. Sendlinger, *J. Less-Common Met.* **1990**, 162(1), L17.
- [5] M. Wörle, H. Meyer zu Altenschild, R. Nesper, *J. Alloys Compd.* **1998**, 264, 107.
- [6] M. Häberlen, J. Glaser, H.-J. Meyer, *J. Solid State Chem.* **2004**, 178, 1478.
- [7] H. Womelsdorf, H.-J. Meyer, *Z. Anorg. Allg. Chem.* **1994**, 620, 262.
- [8] F.E. Rohrer, *Dissertation*, ETH Zürich **1997**.
- [9] O. Reckeweg, F.J DiSalvo, M. Somer, *J. Alloys Compd.* **2003**, 361, 102.
- [10] M. Somer, U. Herterich, J. Čurda, K. Peters, H.G. von Schnering, *Z. Kristallogr.* **1994**, 209, 617.
- [11] M. Somer, U. Herterich, J. Čurda, K. Peters, H.G. von Schnering, *Z. Kristallogr.* **1994**, 209, 182.
- [12] M. Somer, U. Herterich, J. Čurda, K. Peters, H.G. von Schnering, *Z. Kristallogr.* **1996**, 211, 54.
- [13] M. Somer, U. Herterich, J. Čurda, W. Carrillo-Cabrera, A. Zürn, K. Peters, H.G. von Schnering, *Z. Anorg. Allg. Chem.* **2000**, 626, 625.
- [14] J. Čurda, U. Herterich, K. Peters, M. Somer, H.G. von Schnering, *Z. Kristallogr.* **1994**, 209, 618.

- [15] M. Somer, U. Herterich, J. Čurda, K. Peters, H.G. von Schnering, *Z. Kristallogr.* **1995**, 210, 529.
- [16] M. Somer et al. unpublished results.
- [17] S. S. Ozturk, I. Kokal, M. Somer, *Z. Anorg. Allg. Chem.* **2005**, 220, 303.
- [18] M. Somer, I. Kokal, L. Akselrud, W. Carrillo-Cabrera, 10th European Solid State Conference , Vol.:P-047 , 09 , **2005**, Sheffield-UK
- [19] M. Somer, M. N. Kütükçü, W. Cabrillo-Cabrera, R. Cardoso Gil, H. Borrmann, *Z. Anorg. Allg. Chem.* **2004**, 630, 1015.
- [20] M. Somer, Ö. Yaren, O. Reckeweg, Y. Prots, W. Carillo-Cabrera, *Z. Anorg. Allg. Chem.* **2004**, 630, 1068.
- [21] F.E. Rohrer, R. Nesper, *J. Solid State Chem.* **1998**, 135, 194.
- [22] F.E. Rohrer, R. Nesper, *J. Solid State Chem.* **1999**, 142, 187.
- [23] F.E. Rohrer, R. Nesper, *J. Solid State Chem.* **1999**, 142, 192.
- [24] O. Reckeweg, J. Reiherzer, A. Schulz, F.J Disalvo, *Z. Naturforsch. B.* **2008**, 63, 525
- [25] F. E. Rohrer, Doctoral Thesis, Eidgenössische Technische Hochschule, Zürich, **1997**.
- [26] MBRAUN Technical Guide. **2005**, MBRAUN available at: <http://www.mbraun.de/technical.guide.htm>.
- [27] Inorganic Crystal Structure Database(ICSD). 2005, FIZ Karlsruhe: Germany.
- [28] Stoe WINXPOW 1.2 **2000**, Stoe & Cie GmbH: Darmstadt
- [29] K. D. M. Harris, M. Tremayne, and B. M. Kariuki, *Angewandte Chemie Internatioanl Editon.* **2001**. 40:p 1626-1651.
- [30] G. Sheldrick, SHELXS97, Gottingen, **1997**, Germany.
- [31] G. Sheldrick, SHELXL97-2, Gottingen, **1997**, Germany.
- [32] Thermal Analysis Product and Solutions. **2005**, NETZSCH- Gerätebau GmbH available at: <http://www.netzsch-thermal-analysis.com/en/products/>.

-
- [33] B. Stuart, *Infrared Spectroscopy : Fundamentals and Applications* 1st ed. **2005**: John Wiley & Sons. Inc.
- [34] Jasco, *Model FT/IR-600 Plus Function Manual*.**2001**.
- [35] K. Nakamoto, *Infrared and Raman spectra of inorganic and coordination compounds* 5th ed. Vol.2. **1997**. New York Wiley.
- [36] Bruker, *RFS 100 User Manual*. **2004**.
- [37] G. Vandergrift and B. Fultz *American Journal of Physics* **1998**, 66, 593.
- [38] L. G. Akselrud, P. Y. Zavalli, Yu. N. Grin, V. K. Pecharsky, B. Baumgartner, E. Wölfel, *Mater. Sci. Forum* **1993**, 133-136, 335.
- [39] *Diamond Version 3.1a*, K. Brandenburg, **2007**
- [40] M. Somer, *Z.Naturforsch.*, **1991**, 46b, 1664.
- [41] H. Lueken, *Magnetochemie*, Teubner, Stuttgart, **1999**.
- [42] R. Boese, A. H. Maulitz, P. Stellberg, *Chem. Ber.* **1994**, 127, 1887.
- [43] M. Somer, C. Gül, R. Müllmann, B. D. Mosel,, R. K. Kremer, R. Pöttgen, *Z. Anorg. Allg. Chem.* **2004**, 630, 389.
- [44] T. Aitasola, J.Holsa, M.Lastusaari, J. Jegendziewicz, L. Lehto, J. Linden, M. Marysko, *J. Alloys Compd.* **2004**, 380, 296.

VITA

Ilkin Kokal was born in Balıkesir, Turkey, in 1983. He completed high school in Balıkesir Sırrı Yırcalı Anadolu Lisesi in 2001. He received his B.S. degree in Chemistry from Koc University, İstanbul, in 2005. The same year, he started his Master studies in the program Material Science and Engineering at Koç University He will be pursuing his Ph.D. research at Technical University of Eindhoven, Netherlands. His research interests are nitridoborates and solid state hydrogen storage material.